

Modified propagation of gravitational waves from the early radiation era

Yutong He,^{a,b} Alberto Roper Pol^{c,d,e} and Axel Brandenburg^{a,b,e,f}

^aNordita, KTH Royal Institute of Technology and Stockholm University, Hannes Alfvéns väg 12, SE-10691 Stockholm, Sweden

^bThe Oskar Klein Centre, Department of Astronomy, Stockholm University, AlbaNova, SE-10691 Stockholm, Sweden

^cDépartement de Physique Théorique, Université de Genève, CH-1211 Genève, Switzerland

^dUniversité Paris Cité, CNRS, Astroparticule et Cosmologie, Paris, F-75013, France

^eSchool of Natural Sciences and Medicine, Ilia State University, 3-5 Cholokashvili Ave, Tbilisi, GE-0194, Georgia

^fMcWilliams Center for Cosmology and Department of Physics, Carnegie Mellon University, 5000 Forbes Ave, Pittsburgh, PA 15213, USA
June 21, 2023

E-mail: yutong.he@su.se, alberto.roperpol@unige.ch, brandenb@nordita.org

Abstract. We study the propagation of cosmological gravitational wave (GW) backgrounds from the early radiation era until the present day in modified theories of gravity. Comparing to general relativity (GR), we study the effects that modified gravity parameters, such as the GW friction α_M and the tensor speed excess α_T , have on the present-day GW spectrum. We use both the WKB estimate, which provides an analytical description but fails at superhorizon scales, and numerical simulations that allow us to go beyond the WKB approximation. We show that a constant α_T makes relatively insignificant changes to the GR solution, especially taking into account the constraints on its value from GW observations by the LIGO–Virgo collaboration, while α_M can introduce modifications to the spectral slopes of the GW energy spectrum in the low-frequency regime depending on the considered time evolution of α_M . The latter effect is additional to the damping or growth occurring equally at all scales that can be predicted by the WKB approximation. In light of the recent observations by pulsar timing array (PTA) collaborations, and the potential observations by future detectors such as SKA, LISA, DECIGO, BBO, or ET, we show that, in most of the cases, constraints cannot be placed on the effects of α_M and the initial GW energy density $\mathcal{E}_{\text{GW}}^*$ separately, but only on the combined effects of the two, unless the signal is observed at different frequency ranges. In particular, we provide some constraints on the combined effects from the reported PTA observations.

Contents

1	Introduction	1
2	Modified GWs on FLRW background	3
3	WKB approximation	5
3.1	Solution of the GW equation	5
3.2	Limitations of the WKB approximation	6
3.3	GW spectrum using the WKB approximation	8
4	Phenomenological parameterizations	9
5	Numerical solutions	11
5.1	Initial condition and time stepping schemes	12
5.2	Time evolution	15
5.3	Energy spectrum	17
6	Observational implications	19
7	Conclusions	23
A	Friedmann equations	25
B	GW energy spectrum via WKB approximation	27
C	Numerical scheme	28
D	Numerical accuracy	29

1 Introduction

The present day Hubble constant, H_0 , is measured to be around $H_0 \sim 74$ km/s/Mpc by astrophysical tests using type Ia supernovae [1–3], lensed quasars [4], and megamaser-hosting galaxies [5]. On the other hand, cosmological tests of H_0 constrain its value to $H_0 \sim 67$ km/s/Mpc from cosmic microwave background (CMB) [6] and baryon acoustic oscillations (BAO) [7] experiments, assuming the standard Λ CDM (Λ cold dark matter) model of cosmology. These measurements suggest the presence of a 4–5 σ deviation discrepancy between the early- and late-universe measurements of H_0 [8], known as the Hubble tension. The observation of gravitational waves (GWs) from “standard sirens” provides an independent measurement of the Hubble rate [9, 10]. Current observations from LIGO–Virgo present large uncertainties and cannot yet solve the tension [11–14]. However, the measurement of H_0 is expected to drastically improve with the space-based GW detector LISA [15] or the next-generation ground-based detectors like the Einstein Telescope (ET) [16]. Besides the well-known H_0 tension, a number of other observational discrepancies within the Λ CDM model have been reported, such as the S_8 tension, where $S_8 \propto \sigma_8 \Omega_{\text{mat},0}^{1/2}$ characterizes the structure growth rate

σ_8 and today’s matter density $\Omega_{\text{mat},0}$ [17]. A recent summary of over a dozen cosmological tensions and their varied significance can be found in ref. [18].

In view of these tensions, Λ CDM, although being an extremely successful model, does not provide a complete picture and it might be necessary to go beyond it. Since general relativity (GR) is responsible for the gravity sector of Λ CDM, modifying Λ CDM often requires modifying GR.

In search for modified gravity (MG) theories, certain systematic approaches have been developed to go beyond GR, such as relaxing one or some of the assumptions made in Lovelock’s theorem that proves the uniqueness of GR [19, 20]. Overarching families of MG theories have been constructed to represent a vast number of individual models, for example Horndeski’s theory, which corresponds to all four-dimensional scalar-tensor models with second-order derivatives [21–23], beyond Horndeski [24–26], Degenerate Higher-Order Scalar-Tensor (DHOST) [27–29], Hořava-Lifshitz [30, 31], Generalized Einstein-Aether gravity [32, 33], standard [34, 35] and beyond [36–38] generalized Proca, bimetric gravity [39–41], and tensor-scalar-vector (TeVeS) [42] theories. Some specific examples of MG theories are: Brans-Dicke [43], quintessence [44], $f(R)$ [45], $f(G)$ [46], k -essence [47], kinetic gravity braiding [48], and galileon [49]. For a comprehensive review see, e.g., ref. [50].

At the level of tensor linear perturbations, MG theories introduce three parameters to the standard gravitational wave (GW) equation that can be conveniently used as a phenomenological probe in the parameter space of MG:

- GW friction α_M , usually¹ associated to the running of the effective Planck mass $\alpha_M = d \ln M_{\text{eff}}^2 / d \ln a$. The friction term yields a GW luminosity distance different than the electromagnetic (EM) counterpart $d_{\text{GW}} \neq d_{\text{EM}}$ that allows us to put constraints on $|\alpha_M| \sim \mathcal{O}(10^0)$ [51–56]. Signals propagating over longer distances could provide tighter constraints. Such “standard siren” measurements have so far yielded mild constraints on α_M , as LIGO–Virgo covers a relatively small distance of $z \sim \mathcal{O}(10^{-1})$ [57, 58]. Cosmological tests involving the CMB provide a tighter constraint of $|\alpha_M| \lesssim \mathcal{O}(10^{-1})$ [6] at the present day; see section 4 for details. This aspect can also be improved with LISA [15, 59, 60] and ET [16, 51, 56, 61–63], which might probe distances up to $z \sim \mathcal{O}(10^1)$.
- Tensor speed excess α_T , related to the GW speed c_T via $c_T^2 = \alpha_T + 1$. It has been tightly bounded to $\alpha_T \lesssim \mathcal{O}(10^{-15})$ by the multi-messenger detection of GW170817 and GRB 170817A [64]. This observation in turn constrains the theory space of MG [65–68]. However, this constraint only applies to the frequency range probed by LIGO–Virgo and might not necessarily apply at different frequencies, as proposed in ref. [69].
- Graviton mass m_g , which modifies the otherwise linear dispersion relation in GR.

In this paper, we focus on the study of the modifications on the expected relic cosmological GW spectrum under MG for different time-dependent GW friction models, and for constant values of $\alpha_T \neq 0$. We present the general theoretical framework for time-dependent α_M and α_T , but defer the study of time and/or frequency dependent α_T to future work. For a similar study concerning the effects of m_g , see ref. [70]. Our focus on the cosmological effects of α_M is motivated by its less stringent constraints compared to α_T , and its accumulated effects over cosmic history. We ignore the effects of scalar perturbations in MG that can lead to gravitational slip and focus only on the phenomenological effects on the tensor sector. For

¹This is not necessarily the only interpretation of the GW friction; see, e.g., ref. [51].

the combined study of scalar and tensor perturbations in MG see refs. [53, 63]. Similarly, we ignore modifications on the dark energy equation of state and set $w_{\text{DE}} = -1$ (i.e., $w_0 = -1$ and $w_a = 0$) [6, 71], such that the Λ CDM background expansion is unmodified.

To this end, we initialize a GW spectrum based on previous studies of GWs sourced by primordial magnetohydrodynamic (MHD) turbulent fields in the early radiation era—e.g., at the electroweak or QCD phase transitions (EWPT or QCDPT)—and then propagate it through cosmic history to obtain the present-day relic spectrum. Actually, we take a generic double broken power law GW spectrum and we show that the obtained results are independent of the initial spectral shape. Hence, our results can be applied to predict the expected GW spectrum from a generic source in MG. We then analytically and numerically compare the relic spectra in GR and MG, and discuss their potential observational implications. The numerical solutions in this study are obtained using the PENCIL CODE [72], which has been used as a tool for simulations of GWs from primordial turbulent sources since the implementation of a GW solver [73]. The cosmological history of the universe is modelled by numerically solving Friedmann equations. We provide a cosmological solver and a tutorial within the associated online material [74]. It also contains the routines that have been used to process the data obtained from the PENCIL CODE and to generate the results and plots of the present work.

We introduce the propagation of tensor-mode perturbations described by the GW equation in MG in section 2. In section 3, we introduce the WKB approximation commonly used to describe approximate solutions to the modified GW equation. We derive the WKB solution in section 3.1, study its limitations and range of validity in section 3.2, and compute the GW spectrum in section 3.3. Then, in section 4, we present some common parameterizations of the parameter α_{M} through the history of the universe that have been used in the literature, and we present the numerical simulations that we perform to solve the GW equation using the PENCIL CODE in section 5. In particular, we study the effects on the GW spectrum that can not be predicted using the WKB. In particular, we study the effects on the GW spectrum that cannot be predicted using the WKB approximation. Finally, we discuss potential observational implications of MG compared to GR for the different parameterizations of α_{M} in section 6 and conclude in section 7.

Throughout the paper, we set $c = \hbar = k_{\text{B}} = 1$, use the metric signature $(-+++)$, and define the gravitational coupling constant $\kappa = 8\pi G_{\text{N}}$, where G_{N} is the Newton constant. We indicate with a prime derivatives with respect to conformal time normalized by the conformal Hubble rate at the time of GW generation $\eta\mathcal{H}_*$ and with a dot derivatives with respect to cosmic time t . Both times are related via the scale factor as $a d\eta = dt$.

2 Modified GWs on FLRW background

For simplicity, we assume the background evolution to follow Λ CDM, while allowing a generic modification of the GW evolution. Therefore, we start with the homogeneous and isotropic background described by the Friedmann-Lemaître-Robertson-Walker (FLRW) metric. Including tensor perturbations, the FLRW line element reads

$$ds^2 = a^2(-d\eta^2 + [\delta_{ij} + a^{-1}h_{ij}(\mathbf{x}, \eta)] dx^i dx^j), \quad (2.1)$$

where $h_{ij} = ah_{ij}^{\text{phys}}$ are the strains obtained by scaling the physical strains h_{ij}^{phys} with the scale factor a . In GR, the GW equation in Fourier space² reads [73, 75]

$$\tilde{h}_{ij}''(\mathbf{k}, \eta) + \left(k^2 - \frac{a''}{a}\right) \tilde{h}_{ij}(\mathbf{k}, \eta) = \frac{6}{a} \tilde{T}_{ij}^{\text{TT}}(\mathbf{k}, \eta), \quad (2.2)$$

where $\tilde{T}_{ij}^{\text{TT}} = \Lambda_{ijlm} \tilde{T}_{lm}$ is the traceless-transverse (TT) projection of the normalized stress energy tensor, i.e., divided by the radiation energy density $\mathcal{E}_{\text{rad}} = 3H^2/\kappa$, being $H \equiv \dot{a}/a$ the Hubble rate at time η . The projection operator is $\Lambda_{ijlm}(\hat{\mathbf{k}}) = P_{il}P_{jm} - \frac{1}{2}P_{ij}P_{lm}$, where $P_{ij}(\hat{\mathbf{k}}) = \delta_{ij} - \hat{k}_i\hat{k}_j$ and $\hat{\mathbf{k}} = \mathbf{k}/k$. The scale factor at η_* is set to unity, and the wave numbers k are also normalized by the (normalized) conformal Hubble rate $\mathcal{H} \equiv a'/a$. We use an asterisk to refer to the time in the early universe at which the GWs were generated.

Including the additional parameters α_{M} and α_{T} mentioned in section 1, equation (2.2) generalizes to [76, 77]

$$\tilde{h}_{ij}''(\mathbf{k}, \eta) + \alpha_{\text{M}} \mathcal{H} \tilde{h}_{ij}'(\mathbf{k}, \eta) + \left(c_{\text{T}}^2 k^2 - \alpha_{\text{M}} \mathcal{H}^2 - \frac{a''}{a}\right) \tilde{h}_{ij}(\mathbf{k}, \eta) = \frac{6}{a} \tilde{T}_{ij}^{\text{TT}}(\mathbf{k}, \eta). \quad (2.3)$$

The effect of massive gravitons could be included by adding a $m_{\text{g}} \neq 0$ term multiplying to h_{ij} in equation (2.3), as done in ref. [70], but we omit it in the present work.

Equation (2.3) can be recast in a simplified equation by introducing the new variable $\chi_{ij} = e^{\mathcal{D}} h_{ij}$ [51, 56, 60], with

$$\mathcal{D}(\eta) = \frac{1}{2} \int_1^{\eta \mathcal{H}_*} \alpha_{\text{M}} \mathcal{H} d\tau, \quad (2.4)$$

where the integral is performed over normalized time $\tau = \eta' \mathcal{H}_*$. This yields

$$\tilde{\chi}_{ij}''(\mathbf{k}, \eta) + \left(c_{\text{T}}^2 k^2 - \frac{\tilde{a}''}{\tilde{a}}\right) \tilde{\chi}_{ij}(\mathbf{k}, \eta) = \frac{6}{a} \tilde{T}_{ij}^{\text{TT}}(\mathbf{k}, \eta), \quad (2.5)$$

where $\tilde{a} = ae^{\mathcal{D}}$, and \tilde{a}''/\tilde{a} can be assembled from a and α_{M} as

$$\frac{\tilde{a}''}{\tilde{a}} = \frac{a''}{a} \left(1 + \frac{1}{2}\alpha_{\text{M}}\right) + \frac{1}{2}\alpha_{\text{M}} \mathcal{H}^2 \left(1 + \frac{1}{2}\alpha_{\text{M}}\right) + \frac{1}{2}\alpha_{\text{M}}' \mathcal{H}. \quad (2.6)$$

The variable χ is related to the difference between GW and EM luminosity distances mentioned in section 1. We first express the latter in Λ CDM,

$$d_{\text{EM}} = \frac{a_0}{aH_0} \int_a^{a_0} \frac{a_0 da'}{a'^2 \sqrt{\Omega(a)}}, \quad (2.7)$$

where H_0 is today's Hubble rate and $\Omega(a)$ is the total energy density, which includes matter, radiation, and dark energy contributions; see appendix A. The GW luminosity distance is

$$d_{\text{GW}} = \frac{a}{\tilde{a}} d_{\text{EM}} = e^{-\mathcal{D}} d_{\text{EM}}, \quad (2.8)$$

²We use a tilde for variables in Fourier space and the following convention

$$\tilde{h}(\mathbf{k}) = \int h(\mathbf{x}) e^{-i\mathbf{k}\cdot\mathbf{x}} d^3\mathbf{x}, \quad h(\mathbf{x}) = \frac{1}{(2\pi)^3} \int \tilde{h}(\mathbf{k}) e^{i\mathbf{k}\cdot\mathbf{x}} d^3\mathbf{k}.$$

which reduces to $d_{\text{GW}} = d_{\text{EM}}$ in GR; see ref. [78] for a detailed calculation.

Previous numerical work was usually restricted to specific eras, e.g., radiation (RD) [73, 79–85] or matter domination (MD) [86–88], using a constant equation of state (EOS), defined to be $w \equiv p/\rho$, being p the pressure and ρ the energy density, such that $w = 1/3$ and 0 during RD and MD, respectively. The dynamical thermal history of the universe during RD, represented by the relativistic g_* and adiabatic g_S degrees of freedom, was also ignored. In GR, this formulation is justified since the evolution of the physical strains h_{ij}^{phys} when the source is inactive ($T_{ij} \sim 0$) can be approximated to dilute as $h_{ij}^{\text{phys}} \propto a^{-1}$ if one neglects the evolving relativistic degrees of freedom and transitions between radiation, matter, and dark energy dominations (Λ D) [89]. In the present work, we focus on including such effects and solve the GW equation in modified gravity, which present richer dynamics even when the source is inactive, from the time of GW generation up to present time.

Assuming a piece-wise EOS, such that $w = 1/3$, 0, and -1 during RD, MD, and Λ D, respectively, would create discontinuities in the time evolution of $a(\eta)$ and its derivatives that appear in equations (2.3) and (2.5). Therefore, to find a smooth $a(\eta)$, we directly solve the Friedmann equations (see appendix A for details),

$$\mathcal{H} = \frac{H_0}{\mathcal{H}_*} a \sqrt{\Omega(a)}, \quad \frac{a''}{a} = \frac{1}{2} \mathcal{H}^2 [1 - 3w(a)], \quad (2.9)$$

where $\Omega(a)$ denotes the total energy density, and the term \mathcal{H}_* appears due to our definition of the normalized $\mathcal{H} = a'/a$. We set $a_* = 1$ for consistency with our GW equation; see the discussion below equation (2.2). Using equation (2.9), we solve for the time evolution of the scale factor $a(\eta)$ and finally obtain the time evolution of \mathcal{H} and a'' that are required to solve the GW equation, either when they appear explicitly in equation (2.3) for h_{ij} or to compute the term \tilde{a}'' , defined in equation (2.6), that appears in equation (2.5) for χ_{ij} .

3 WKB approximation

3.1 Solution of the GW equation

Modifications of the GW propagation, in the absence of sources³ (i.e., $T_{ij} = 0$), have been studied using the WKB approximation [55, 59]. The WKB solution can be obtained using the following ansatz

$$\tilde{\chi}_{ij}(k, \eta) = \chi(k, \eta) e_{ij} = A e_{ij} e^{iB}, \quad (3.1)$$

where A and B are generic coefficients, and e_{ij} is the polarization tensor.⁴ Substituting this into equation (2.5), one gets

$$0 = 2 \frac{A'}{A} + \frac{B''}{B'} \Rightarrow A(\eta) = e^{-\tilde{D}}, \quad (3.2)$$

$$B'^2 = \frac{A''}{A} + k^2 c_T^2 - \frac{\tilde{a}''}{\tilde{a}} \approx k^2 c_T^2 \Rightarrow B(k, \eta) = \pm k(\eta \mathcal{H}_* - \Delta T), \quad (3.3)$$

³In the absence of sources, the GW equation [see equation (2.3)] does not depend on the wave vector \mathbf{k} but only on its modulus (the wave number) k . Hence, the solution can simply be expressed as a function of k .

⁴In the absence of sources, the GW propagation of any polarization mode is the same, so we can just call χ the amplitude of each mode. If the produced GW signal is polarized, then for each mode we need to impose the corresponding initial conditions.

where we have neglected A''/A and \tilde{a}''/\tilde{a} compared to $k^2 c_{\text{T}}^2$, following the WKB approximation. We have defined the additional damping factor $\tilde{\mathcal{D}}$, and the time delay due to the effective GW speed ΔT

$$\tilde{\mathcal{D}} = \frac{1}{2} \int_1^{\eta \mathcal{H}_*} \frac{B''}{B'} d\tau = \frac{1}{2} \int_1^{\eta \mathcal{H}_*} \frac{c_{\text{T}}'}{c_{\text{T}}} d\tau, \quad \Delta T = \int_1^{\eta \mathcal{H}_*} (1 - c_{\text{T}}) d\tau. \quad (3.4)$$

Hence, the particular solution is

$$\chi(k, \eta) = e^{-\tilde{\mathcal{D}}} e^{\pm i k (\eta \mathcal{H}_* - \Delta T)} = e^{-\tilde{\mathcal{D}} \mp i k \Delta T} \chi^{\text{GR}}(k, \eta). \quad (3.5)$$

where $\tilde{\mathcal{D}} = \Delta T = 0$ in GR. For the initial conditions⁵ $\chi(k, \eta_*) = \chi_*(k)$ and $\chi'(k, \eta_*) = \chi'_*(k)$, the general solution reads

$$\chi(k, \eta) = e^{-\tilde{\mathcal{D}}} \left[\chi_*(k) \cos k \tilde{c}_{\text{T}}(\eta \mathcal{H}_* - 1) + \frac{c_{\text{T}}^* \chi'_*(k) + \frac{1}{2} c_{\text{T}}'^* \chi_*(k)}{k c_{\text{T}}^{*2}} \sin k \tilde{c}_{\text{T}}(\eta \mathcal{H}_* - 1) \right], \quad (3.6)$$

where $\tilde{c}_{\text{T}}(\eta) = \int c_{\text{T}} d\eta' / (\eta \mathcal{H}_* - 1)$, and c_{T}^* and $c_{\text{T}}'^*$ are the values of the GW speed (and its derivative) at the initial time of GW production. Note that the specific choice of initial conditions does not allow to give a linear relation between χ and χ^{GR} as done in ref. [55] and, in general, $\chi \neq e^{-\tilde{\mathcal{D}} - i k \Delta T} \chi^{\text{GR}}$, which is only true when referring to the particular solution of the ODE, given in equation (3.5). In terms of the initial conditions $h(k, \eta_*) = h_*(k) = \chi_*(k)$ and $h'(k, \eta_*) = h'_*(k) = \chi'_*(k) - \frac{1}{2} \alpha_{\text{M}}^* \chi_*(k)$, the solution (3.6) can be rewritten as

$$\chi(k, \eta) = e^{-\tilde{\mathcal{D}}} \left[h_*(k) \cos k \tilde{c}_{\text{T}}(\eta \mathcal{H}_* - 1) + \frac{c_{\text{T}}^* h'_*(k) + \frac{1}{2} (c_{\text{T}}^* \alpha_{\text{M}}^* + c_{\text{T}}'^*) h_*(k)}{k c_{\text{T}}^{*2}} \sin k \tilde{c}_{\text{T}}(\eta \mathcal{H}_* - 1) \right]. \quad (3.7)$$

The general solution reduces to the following when $c_{\text{T}} = 1$ at all times,

$$\chi(k, \eta) = h_*(k) \cos k (\eta \mathcal{H}_* - 1) + \frac{h'_*(k) + \frac{1}{2} \alpha_{\text{M}}^* h_*(k)}{k} \sin k (\eta \mathcal{H}_* - 1). \quad (3.8)$$

This expression holds both in GR with $h(k, \eta) = \chi(k, \eta)$ and $\alpha_{\text{M}} = 0$, and in MG theories with $h(k, \eta) = e^{-\mathcal{D}} \chi(k, \eta)$ and $\alpha_{\text{M}} \neq 0$.

3.2 Limitations of the WKB approximation

To obtain the WKB solution, we have neglected two terms in equation (3.3), which can be expressed as

$$\frac{A''}{A} - \frac{\tilde{a}''}{\tilde{a}} = -\frac{c_{\text{T}}''}{2c_{\text{T}}} + \frac{3c_{\text{T}}'^2}{4c_{\text{T}}^2} - \frac{1}{2} \alpha_{\text{M}} \left(1 + \frac{1}{2} \alpha_{\text{M}} \right) \mathcal{H}^2 - \frac{1}{2} \alpha_{\text{M}}' \mathcal{H} - \frac{a''}{a} \left(1 + \frac{1}{2} \alpha_{\text{M}} \right), \quad (3.9)$$

where we have used $\mathcal{H}' = a''/a - \mathcal{H}^2$. Hence, the WKB assumption could break down when at least one of these terms is not negligible when compared to $k^2 c_{\text{T}}^2$. First, we obtain the

⁵In the current work, we focus on the propagation of a GW background after it has already been generated and reached a stationary solution, when the source is no longer active. Since the propagation only depends on k , the initial conditions can be computed from the 3D fields in Fourier space, after shell integration over directions \hat{k} , for each polarization mode.

limiting values of k due to c_T and its derivatives in the first two terms on the right-hand side of equation (3.9)

$$k_{\text{lim},c_T''} \lesssim \sqrt{\frac{|c_T''|}{2c_T^3}}, \quad k_{\text{lim},c_T'} \lesssim \frac{\sqrt{3}|c_T'|}{2c_T^2}. \quad (3.10)$$

Note that in this paper we only consider c_T to be constant in time, i.e., $k_{\text{lim},c_T''}$ and $k_{\text{lim},c_T'}$ are zero. We defer the study of time-varying c_T and its effects to future work.

In addition, we have one term that depends on α_M , one term that depends on the time evolution of α_M , and one term that depends on a''/a . The latter appears also in GR when WKB is used to approximate the solution for the scaled strains, which do not decay (note that the decay of the physical strains is already absorbed by the scale factor), as shown in equation (3.8). This term is given in equation (2.9) and its upper bound can be found using Friedmann equations

$$\frac{a''}{a} \lesssim \frac{1}{2} \frac{\Omega_{\text{mat},0}}{\Omega_{\text{rad},0}} \frac{g_*}{g_*^0} \left(\frac{g_S}{g_S^0} \right)^{-\frac{4}{3}} \mathcal{H} \frac{a_*}{a_0} \lesssim 10^4 h^2 \mathcal{H} \frac{a_*}{a_0}, \quad (3.11)$$

where the first inequality is an approximation valid during the RD era and it decays during MD. Hence, the upper bound is valid at all times and its specific value depends on a_*/a_0 . For example, for GWs generated at the EWPT or at the QCDPT, this leads to the following limiting wave numbers (for $h = 0.67$), at which the WKB approximation might break down,

$$k_{\text{lim},a''}^{\text{EW}} \sim 1.87 \times 10^{-6} \mathcal{H} \sqrt{\frac{|1 + \frac{1}{2}\alpha_M|}{c_T}} \leq 1.87 \times 10^{-6} \sqrt{\frac{|1 + \frac{1}{2}\alpha_M|}{c_T}}, \quad (3.12)$$

$$k_{\text{lim},a''}^{\text{QCD}} \sim 5.90 \times 10^{-5} \mathcal{H} \sqrt{\frac{|1 + \frac{1}{2}\alpha_M|}{c_T}} \leq 5.90 \times 10^{-5} \sqrt{\frac{|1 + \frac{1}{2}\alpha_M|}{c_T}}. \quad (3.13)$$

In both cases, this term is subdominant up to very large superhorizon scales and it is bounded by the values in equations (3.12) and (3.13) since $\mathcal{H} = \eta_*/\eta$ during RD era as can be seen using equation (2.9). This limit can be modified by the inclusion of α_M and α_T but unless they take large values these modifications are negligible.

On the other hand, two additional limitations to the WKB approximation appear due to the α_M parameter,

$$k_{\text{lim},\alpha_M} \sim \frac{\mathcal{H}}{c_T} \sqrt{\left| \frac{\alpha_M}{2} \left(1 + \frac{1}{2}\alpha_M \right) \right|} \lesssim \frac{1}{c_T} \sqrt{\frac{|\alpha_M^*|}{2}}, \quad (3.14)$$

$$k_{\text{lim},\alpha_M'} \sim \frac{1}{c_T} \sqrt{\frac{\mathcal{H}|\alpha_M'|}{2}} \leq \frac{1}{c_T} \sqrt{\frac{|\alpha_M'^*|}{2}}, \quad (3.15)$$

where we can neglect the term $\frac{1}{2}\alpha_M$ in front of 1 in the first limit for small values of α_M . Hence, the WKB limit can break down in MG around the horizon or at larger scales. In general, we expect the limit from α_M to be more restrictive than that from α_M' and to dominate at the initial time when $\mathcal{H} = 1$. However, this depends on the parameterization of α_M , which can give different results for both limits; see section 4.

3.3 GW spectrum using the WKB approximation

The spectrum of GW energy density can be expressed as

$$\Omega_{\text{GW}}(k, \eta) = \frac{1}{\rho_{\text{crit},0}} \frac{d\rho_{\text{GW}}}{d \ln k} = \frac{1}{6} \left(\frac{H_*}{H_0} \right)^2 \left(\frac{a_*}{a_0} \right)^4 k S_{h'}(k, \eta), \quad (3.16)$$

where $2S_{h'}$ is the spectrum⁶ of the scaled strain derivatives,

$$\langle \tilde{h}'_{ij}(\mathbf{k}, \eta) \tilde{h}'_{ij}{}^*(\mathbf{k}', \eta) \rangle = (2\pi)^6 \delta^3(\mathbf{k} - \mathbf{k}') \frac{2S_{h'}(k, \eta)}{4\pi k^2}. \quad (3.17)$$

Taking $\mathcal{D}' = \frac{1}{2}\alpha_{\text{M}}\mathcal{H}$, the modified GW energy spectrum can be obtained using the WKB solution for MG, given in equation (3.6), and assuming that at time η_* the GWs are in the free-propagation regime following GR, such that $|h'_*(k)| = k|h_*(k)|$,

$$\Omega_{\text{GW}}(k, \eta) = e^{-2\mathcal{D}} \Omega_{\text{GW}}^{\text{GR}}(k, \eta) \xi(k, \eta), \quad (3.18)$$

where $\xi(k, \eta)$ corresponds to the spectral modifications with respect to the GR spectrum after taking into account the amplification (or depletion) produced by the damping factor \mathcal{D} and assuming constant-in-time c_{T} (see appendix B for details and, in particular, equation (B.9) for generic time-dependent c_{T}),

$$\xi(k, \eta) = 1 + \frac{1}{2}\alpha_{\text{T}} + \frac{\alpha_{\text{M}}^*}{2k} + \frac{1}{8k^2} \left[\alpha_{\text{M}}^2 \mathcal{H}^2 \left(1 + \frac{1}{c_{\text{T}}^2} \right) + \alpha_{\text{M}}^{*2} \right] + \frac{\alpha_{\text{M}}^* \alpha_{\text{M}}^2 \mathcal{H}^2}{8k^3 c_{\text{T}}^2} + \frac{\alpha_{\text{M}}^{*2} \alpha_{\text{M}}^2 \mathcal{H}^2}{32k^4 c_{\text{T}}^2}. \quad (3.19)$$

Note that we have averaged over oscillations in time η , such that the expression is valid at $k \tilde{c}_{\text{T}} \gtrsim (\eta \mathcal{H}_* - 1)^{-1}$. At late times, $\mathcal{H}^2 = (\eta_*/\eta)^2$ becomes small, so we can neglect the terms that dilute with \mathcal{H}^2 ,

$$\xi(k, \eta \gg \eta_*) = \frac{1}{2}(1 + \alpha_{\text{T}}) + \frac{1}{2} \left(1 + \frac{\alpha_{\text{M}}^*}{2k} \right)^2. \quad (3.20)$$

From equation (3.20), we can identify the IR and UV limiting ranges of the spectrum,

$$\Omega_{\text{GW}}^{\text{IR}} = \Omega_{\text{GW}} \left(k \ll \frac{1}{2}\alpha_{\text{M}}^*, \eta \gg \eta_* \right) = \frac{\alpha_{\text{M}}^{*2}}{8k^2} e^{-2\mathcal{D}} \Omega_{\text{GW}}^{\text{GR}}(k, \eta), \quad (3.21)$$

$$\Omega_{\text{GW}}^{\text{UV}} = \Omega_{\text{GW}} \left(k \gg \frac{1}{2}\alpha_{\text{M}}^*, \eta \gg \eta_* \right) = \left(1 + \frac{1}{2}\alpha_{\text{T}} \right) e^{-2\mathcal{D}} \Omega_{\text{GW}}^{\text{GR}}(k, \eta). \quad (3.22)$$

Note that the factor α_{M}^{*2} is part of the IR limit, indicating that the IR enhancement of the form k^{-2} holds regardless of the sign of α_{M}^* . The critical $k_{\text{crit}} = \frac{1}{2}|\alpha_{\text{M}}^*|$ indicates where the IR regime begins, i.e., where the k^{-2} term in equation (3.20) becomes dominant.

Equation (3.19) shows that the GW spectrum in the IR regime can present up to k^{-4} modifications to the GR spectrum but this and other terms vanish as time evolves since they are proportional to \mathcal{H}^2 . Hence, at late times, we end up with the GR spectrum amplified (or diluted) for negative (or positive) \mathcal{D} by $e^{-2\mathcal{D}}$ at all wave numbers with a k^{-2} enhancement

⁶Following ref. [73], we define the spectrum $S_{h'}(k, \eta)$ from the + and \times polarization modes, giving an extra factor of 2 due to the property

$$\tilde{h}'_{ij}(\mathbf{k}, \eta) \tilde{h}'_{ij}{}^*(\mathbf{k}', \eta) = 2[h'_+(\mathbf{k}, \eta) h'_+{}^*(\mathbf{k}', \eta) + h'_\times(\mathbf{k}, \eta) h'_\times{}^*(\mathbf{k}', \eta)].$$

in the IR regime, proportional to the additional $\frac{1}{8}\alpha_M^*$ factor, as shown in equation (3.21). In the UV regime, we find the $e^{-2\mathcal{D}}$ enhancement (or depletion) and an additional factor $1 + \frac{1}{2}\alpha_T$, which is, in general, a function of η . The sign of α_T determines if the GW spectrum is amplified or decreased with respect to that obtained from GR.

We have found that, according to the WKB approximation, the parameter α_M introduces changes in the spectral shape at $k \leq k_{\text{crit}} = \frac{1}{2}|\alpha_M^*|$ that do not dilute as time evolves and depend on the value of α_M only at the time of GW generation. On the other hand, note that, using equations (3.14) and (3.15), we can estimate the WKB approximation to break down around $k \sim \max(k_{\text{lim}, \alpha_M}, k_{\text{lim}, \alpha'_M})$. This means that when $\mathcal{H} \sim 1$, the spectral changes occur at wave numbers around and below the critical k_{crit} , where the WKB approximation might not be valid (for $c_T \sim 1$).

We investigate the resulting spectra in MG using numerical simulations in section 5 with the objective to test the validity of the WKB approximation and its potential limitations and to confirm the resulting GW spectra when MG parameters are introduced.

4 Phenomenological parameterizations

In section 3.3, we noted that, according to the WKB approximation, a constant $\alpha_T \neq 0$ induces modifications in the total GW energy density, but not in its spectral shape as long as $\alpha_T \ll 1$. Realistically, the tensor speed excess at the present day is observationally constrained to be $\alpha_{T,0} \lesssim \mathcal{O}(10^{-15})$ by the binary neutron star merger GW170817 and its gamma-ray burst GRB 170817A [64]. This constraint can be circumvented if α_T is either frequency- or time-dependent, such that larger deviations could hide outside the LIGO–Virgo frequency band [69, 90] or in the past [91, 92]. In this study, we show that even using larger values of α_T , constant in time and frequency, the modifications to the GW spectrum are negligible, which is seen from the WKB approximation and can be confirmed with numerical simulations. Hence, from now on, we will focus on two cases: (i) constant α_T with $\alpha_M = 0$, and (ii) $\alpha_T = 0$ allowing α_M to take different values as a function of time.

In particular, we are interested in the perspectives of negative values of α_M , as they would enhance the amplitude of the GW spectrum. Various constraints on the present-day value $\alpha_{M,0}$ exist in the literature, but are significantly less stringent than those on α_T . Assuming the cosmic acceleration due to scalar-tensor theories of gravity, it can be shown that $|\alpha_M| \lesssim 0.5$ at late times (see figure 4 in ref. [54]). This is compatible with the numerical results of ref. [59] (see their figure 2), giving $|\alpha_{M,0}| \lesssim 1$. On the other hand, the Planck Collaboration reports a slightly tighter constraint on $\alpha_{M,0} \gtrsim -0.1$ (see table 8 of ref. [6]). Note that they parameterize $\alpha_M = \alpha_{M,0} (a/a_0)^n$ with $n \in (0.5, 1)$. In addition, to avoid having an infinite number of GW sources in the early Universe, d_{GW} is required to increase monotonically at earlier times, i.e., $d(d_{\text{GW}})/da \leq 0$, as argued in ref. [57]. Hence, using equations (2.7)–(2.8), one gets a bound for α_M ,

$$\alpha_M(a) \geq \frac{a_0}{a\sqrt{\Omega(a)}} \left[\int_a^{a_0} \frac{a_0 da'}{a'^2 \sqrt{\Omega(a')}} \right]^{-1} - 1, \quad (4.1)$$

which is satisfied by all positive values of α_M and for negative values with $|\alpha_M| \leq |\alpha_M(a_*)| \lesssim 1$. Taking these different constraints into account, we explore a range of $\alpha_{M,0} \in [-0.5, 0.3]$.

Besides the simplest consideration of a constant α_M in time, which we call choice 0, its time-dependent forms can be written in accordance with specific gravity models [93]. Following refs. [77, 94, 95], we choose phenomenological forms of α_M as simplified parameterizations

motivated by effective descriptions of modified gravity [96]. Specifically:

$$\alpha_M(\eta) = \begin{cases} \alpha_{M,0} \left[\frac{a(\eta)}{a_0} \right]^n & \text{(choice I),} \\ \alpha_{M,0} \frac{1}{\Omega(\eta)} & \text{(choice II),} \\ \alpha_{M,0} \frac{1 - \Omega_{\text{mat}}(\eta)/\Omega(\eta)}{1 - \Omega_{\text{mat},0}} & \text{(choice III),} \end{cases} \quad (4.2)$$

where choices II and III give a value of α_M proportional to the percentage of dark energy density and the combination of dark and radiation energy densities, respectively, at each time η compared to their relative amounts at the present time. The exponent n in choice I needs to satisfy the following stability conditions [97]:

$$\text{stability for: } \begin{cases} 0 < n < \frac{3}{2} \Omega_{\text{mat},0} \simeq \frac{1}{2}, & \text{if } \alpha_{M,0} > 0, \\ n > \frac{3}{2}, & \text{if } \alpha_{M,0} < 0. \end{cases} \quad (4.3)$$

To provide an intuition on the aforementioned α_M parameterizations, we show in figure 1 (left panel), for the different time dependencies given in equation (4.2), the evolution of $\alpha_M \mathcal{H}$, which characterizes the growth or damping produced by α_M , according to the WKB approximation [see equation (3.4)]. We also show the time evolutions of $k_{\text{lim}, \alpha_M} c_T$ and $k_{\text{lim}, \alpha'_M} c_T$ (right panel), which correspond to the wave numbers at which the WKB approximation might break down, according to equations (3.14) and (3.15). Figure 1 shows the time evolution from the time of generation (e.g., EWPT) up to present time. We see that for choices 0 and III, $\alpha_M \mathcal{H}$ converges to the same values during RD and Λ D, and only becomes different during MD, as expected. On the other hand, for choices I and II, $\alpha_M \mathcal{H}$ is negligible for all of RD and most of MD and rapidly increases later on, especially during Λ D. For all parameterizations, the GW friction converges to the value $\alpha_{M,0}$ at present time.

We see in figure 1 (right panel) that for choices 0 and III, the limiting k is around the horizon scale at the time of generation, i.e., $k_{\text{lim}, \alpha_M} c_T \sim \sqrt{\alpha_M^*/2}$ and then it decreases into superhorizon scales since it is proportional to $\mathcal{H} = \eta_*/\eta$ (this is because for these choices, $\alpha_M \simeq \alpha_M^*$ during the RD era). The term $\alpha'_M = 0$ for choice 0 and $\alpha'_M \ll \alpha_M$ for choice III, as can be seen in figure 1. The ratio between α'_M and α_M at the time of GW generation, within RD, can be found to be (see the associated online material [74])

$$\left(\frac{|\alpha'_M|}{\alpha_M} \right)_{\text{III}}^{\frac{1}{2}} \lesssim \left[\frac{\Omega_{\text{mat},0} g_* \left(\frac{g_S}{g_S^0} \right)^{-\frac{4}{3}} a_*}{\Omega_{\text{rad},0} g_*^0 \left(\frac{g_S^0}{g_S} \right) a_0} \right]^{\frac{1}{2}} \lesssim \sqrt{2} \times 10^2 h \left(\frac{a_*}{a_0} \right)^{\frac{1}{2}}, \quad (4.4)$$

which only becomes of order 1 when the time of GW generation is around the end of the RD era (see right panel of figure 1). For choices I and II, although the two terms are of the same order, $\alpha'_M \sim \alpha_M^*$, their value at the time of GW generation is much smaller than $\alpha_{M,0}$ (for all $n > 0$ in the choice I). Therefore, for choices 0 and III, the WKB estimate might break down around the horizon and at superhorizon scales, while for choices I and II, the approximation is estimated to be valid also at superhorizon scales (down to the limiting wave number). Hence, for the latter, we do not expect to observe any relevant spectral change, since the IR enhancement is determined by the value of α_M^* , as seen in equation (3.20).

Note that, since many efforts of modifying gravity are aimed at addressing the late-time acceleration of the universe, the α_M parameterization choices are commonly constructed to be

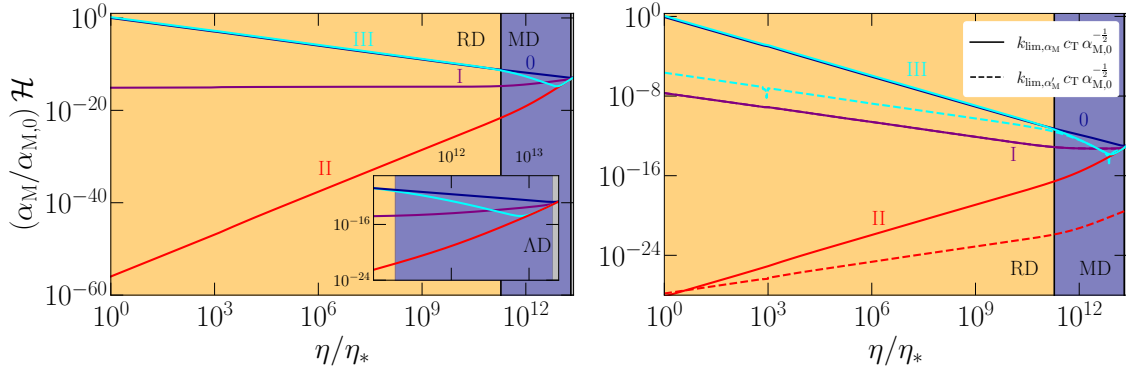


Figure 1: Time evolution of $(\alpha_M/\alpha_{M,0})\mathcal{H}$ (left panel), which contributes to the change of amplitude over time, $h_{ij} \sim e^{-\mathcal{D}}$ with $\mathcal{D} = \frac{1}{2} \int^\eta \alpha_M \mathcal{H} d\eta'$, and of $k_{\text{lim}, \alpha_M} c_T$ and $k_{\text{lim}, \alpha'_M} c_T$ (right panel), which are the terms neglected when compared to $k c_T$ under the WKB approximation; see equations (3.14) and (3.15). All four parameterization choices (0 to III) are shown and, for illustrative purposes, $n = 1$ is chosen. The main figures show the full evolution whereas the inset (in left panel) shows only times after the onset of MD. We have taken η_* to correspond to the EWPT for the specific values in the axes, which puts the present time at $\eta_0/\eta_* \simeq 2.4 \times 10^{13}$.

dominant in the late universe. This is indeed the case for choices I and II here. If one considers only the MD and Λ D history of the universe, choice III is also well-motivated to be relevant at late times. However, here we explore the entire history of the universe from well within RD, which means that $\alpha_M \mathcal{H}$ becomes dominant for choice III both at early and late times. We note that the physical motivations of the choices here can be potentially ambiguous. Even though there exists a wide range of discussions on MG during inflation [77, 98] and around recombination [99, 100], where α_M is essentially a free function of the scalar field, there seems to be a relative lack of numerical studies on the effects of α_M during RD (note, however, a brief discussion of $\alpha_M = -1$ during RD in ref. [101]). Hence, we emphasize the aim of this work to provide an understanding of the phenomenological behavior of the GW spectrum due to α_M for signals produced during RD, although the GW background computed in section 3.3 for MG is relevant in the most general case.

5 Numerical solutions

To explore the limits and validity of the WKB approximation, we use the PENCIL CODE to numerically solve the GW equation under MG, given in equation (2.3). The PENCIL CODE is a highly parallelized modular code that can be used to solve various differential equations [72]. In the context of cosmological GWs, it has previously been used to study GWs generated by hydrodynamic and MHD stresses in the early universe [79]. It uses a GW solver that advances the strains at each time step sourced by the anisotropic stresses that are separately computed as the solution to the MHD equations [73]. Previous numerical work solved the GW equation under GR while, in the present work, we have extended the code to solve equation (2.3); see appendix C for further details on the numerical scheme.

5.1 Initial condition and time stepping schemes

In the current work, we focus primarily on the propagation rather than the production of GWs. Therefore, we have adapted the PENCIL CODE to evolve an initial GW spectrum in the absence of sources with a spectral shape and amplitude based on those obtained in previous studies (see, e.g., refs. [70, 84]). Hence, equation (2.3) is solved in one dimension (i.e., in $k > 0$) in order to improve the efficiency of the code when studying the propagation of a GW background along the history of the universe. We take the initial spectrum for the time derivative of the strains, defined in equation (3.17), to be a smoothed double broken power law described by

$$S_{h'}(k, \eta_*) = S_{h'}^* \frac{\left[1 + \left(\frac{k_*}{k_b}\right)^{a-b}\right] \left(\frac{k}{k_*}\right)^a}{\left[1 + \left(\frac{k}{k_b}\right)^{(a-b)\alpha_1}\right]^{\frac{1}{\alpha_1}} \left[1 + \left(\frac{k}{k_*}\right)^{(b+c)\alpha_2}\right]^{\frac{1}{\alpha_2}}}, \quad (5.1)$$

where $S_{h'}^*$ and k_* are approximately the initial amplitude and position of the peak, respectively, $\eta_* \approx \mathcal{H}_*^{-1}$ corresponds to the time of GW production during the RD era, and $\alpha_1 = \alpha_2 = 2$ are fixed smoothness parameters. We similarly initialize the spectrum of the strains $S_h(k, \eta_*) = S_{h'}(k, \eta_*)/k^2$. We choose the slope in the IR range to be k^2 , set by $a = 2$ (as is expected for causal sources of GWs like the ones produced during a phase transition) up to the break wave number $k_b = 1$, which corresponds to the horizon scale. At intermediate wave numbers, $k_b \leq k \leq k_*$, the slope becomes $b = 0$ as found, for example, for MHD turbulence in refs. [79, 84, 85], followed by the power law $k^{-\frac{11}{3}}$ in the UV range, set by $c = \frac{11}{3}$. This corresponds to the spectrum obtained for Kolmogorov-like MHD turbulence [79]. Note, however, that this part of the spectrum corresponds to subhorizon scales, which are described accurately by the WKB approximation and, hence, the resulting spectral shape is not expected to be modified in this range. On the other hand, around the horizon or at larger scales, depending on the value of α_M^* , the resulting GW spectral shape might be modified by the inclusion of an additional IR branch $\xi^{\text{WKB}}(k) \sim k^{-2}$ as predicted in section 3.3 by the WKB approximation. Finally, the resulting spectrum is expected to be enhanced at all wave numbers by a factor $e^{-2\mathcal{D}}(1 + \frac{1}{2}\alpha_T)$ owing to the presence of non-zero MG parameters α_M and α_T . Figure 2 shows the resulting GW spectrum estimated using the WKB approximation for different values of α_M^* . Note, however, that the assumptions made by the WKB approximation break down around the critical wave number at which we expect the relevant spectral modifications.

Table 1 summarizes the parameters of the runs for the numerical studies. The values of $\alpha_{T,0}$ are chosen to be much larger than the current constraints in order to later show the relative insignificance of $\alpha_{T,0}$ even when it takes large values. The choices of $\alpha_{M,0}$ are made in line with the limits discussed in section 4. For the choice II of α_M parameterization, we take $n = 2$ for negative values of $\alpha_{M,0}$ and $n = 0.4$ for positive values to ensure that the stability conditions of equation (4.3) hold.

For series T0 (T0A–T0D), we evolve the solution entirely with increasing time steps, such that $\eta_{\text{next}} = \eta_{\text{current}}(1 + \delta n_{\text{incr}})$ with $\delta n_{\text{incr}} = 0.01$, leading to equidistant points in logarithmic time spacing. For series M0 (M0A–M0F), M1 (M1A–M1D), M2 (M2A–M2D), and M3 (M3A–M3F), we keep the nonuniform time scheme during RD and MD but switch to linear time steps during Λ D such that $\eta_{\text{next}} = \eta_{\text{current}} + \delta\eta$ with $\delta\eta \mathcal{H}_* = 5 \times 10^9$. We choose such time evolution to improve the accuracy of late-time results for the cases of time-dependent α_M , especially the modifications that they present in the IR limit. We show in

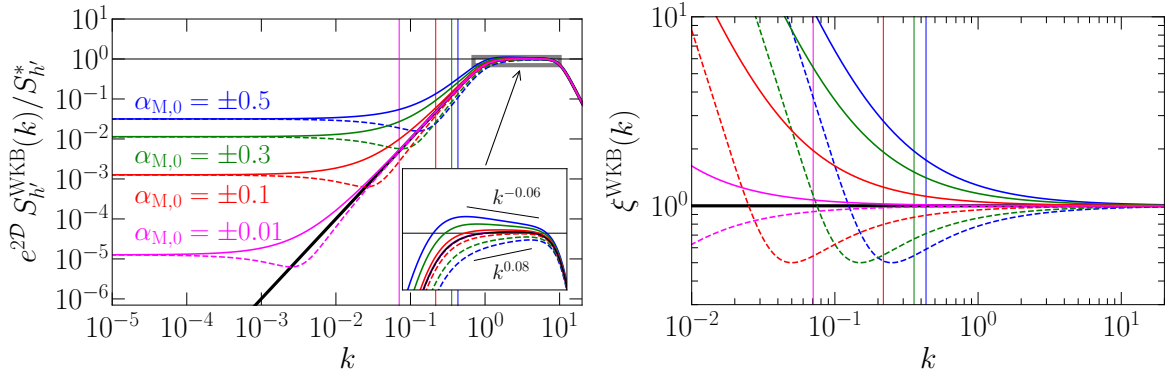


Figure 2: *Left panel:* Expected WKB spectra [see equation (3.18)] of the strain derivatives $S_{h'}(k)$, compensated by e^{-2D} , at late times due to non-zero α_M^* at the time of generation for an initial GW background characterized by a double broken power law, given in equation (5.1). The horizontal line shows the value at the peak $S_{h'}^*$. *Right panel:* Expected spectral modifications $\xi^{\text{WKB}}(k) \equiv e^{2D} S_{h'}^{\text{WKB}}(k) / S_{h'}^{\text{GR}}(k)$, given in equation (3.20). The black curves indicate the GR solution and the colored curves correspond to different values of α_M^* , with the solid and dashed ones being positive and negative values, respectively. Vertical lines indicate the estimated value of k_{lim, α_M} , below which the WKB approximation might fail. The inset zooms in on the behaviors around the horizon at $k \in (1, 10)$.

appendix D that decreasing the time step below $\delta\eta\mathcal{H}_* = 5 \times 10^9$ does not affect the IR range of the spectra, which indicates that the observed modifications are not due to numerical inaccuracy. Since series T0 does not exhibit k -dependent modifications, it does not require the additional computational effort. The choice of time schemes and their numerical accuracy is further discussed in appendix D.

In the simulations, we consider the initial time to be the EWPT with a temperature scale $T_* \sim 100$ GeV and the number of relativistic and adiabatic degrees of freedom are $g_S \approx g_* \sim 100$, which yields the values of a_* and \mathcal{H}_* in equations (A.8) and (A.9). With these values, we can then solve equation (2.3) in units of the normalized time $\eta\mathcal{H}_*$, by mapping the parameterizations in equation (4.2) $\alpha_M(\eta) \rightarrow \alpha_M(\eta/\eta_*)$ and using the results from Friedmann equations for \mathcal{H} and a''/a (which are already normalized since a' is computed as the derivative with respect to $\eta\mathcal{H}_*$), given in equation (2.9). The effects on $S_{h'}(k, \eta)$ of the specific choice of the time at which the GWs are generated only appear via the relative magnitude of the terms a''/a and α_M' that involve time derivatives compared to k . These terms have been parameterized in equations (3.11) and (4.4), respectively, and their magnitude has been discussed. We have shown that the term a''/a can only induce modifications to the solution at scales several orders of magnitude above the horizon scale, while α_M' is only of the order of α_M for choice III (see section 4) at very late times within the RD era. For other choices of $\alpha_M(\eta)$, either $\alpha_M' = 0$ (choice 0) or α_M itself is orders of magnitude below its present-time value $\alpha_{M,0}$ (choices I and II). We find that the WKB approximation is expected to be valid around $k \gg k_{\text{lim}, \alpha_M} \sim \sqrt{|\alpha_M^*|}/2$ and, on the other hand, it predicts an enhancement k^{-2} in the IR regime $k \lesssim k_{\text{crit}} \leq k_{\text{lim}, \alpha_M}$, which is not on the range of validity of the WKB estimate. Using the results of the numerical simulations, we find in section 5.3 an IR enhancement $\xi(k) \propto k^{-\beta_0}$ with $\beta_0 \sim 2$ and $\beta_0 \gtrsim 0$ for negative and positive values of $\alpha_{M,0}$, respectively, that does not in general follow the spectral shape predicted by WKB and that can become

	run	$\alpha_{M,0}$	n	$\alpha_{T,0}$	$\mathcal{E}_{\text{GW}}/\mathcal{E}_{\text{GW}}^*$
Choice 0 (α_T)	T0A	0	–	–0.5	7.50×10^{-1}
	T0B	0	–	–0.2	9.00×10^{-1}
	T0C	0	–	0.2	1.10×10^0
	T0D	0	–	0.5	1.25×10^0
Choice 0 (α_M)	M0A	–0.5	–	0	3.44×10^7
	M0B	–0.3	–	0	3.32×10^4
	M0C	–0.1	–	0	3.21×10^1
	M0D	–0.01	–	0	1.41×10^0
	M0E	0.1	–	0	3.11×10^{-2}
	M0F	0.3	–	0	3.03×10^{-5}
Choice I (α_M)	M1A	–0.5	2	0	1.28×10^0
	M1B	–0.3	2	0	1.16×10^0
	M1C	–0.1	2	0	1.05×10^0
	M1D	0.1	0.4	0	7.79×10^{-1}
	M1E	0.3	0.4	0	4.73×10^{-1}
Choice II (α_M)	M2A	–0.5	–	0	1.32×10^0
	M2B	–0.3	–	0	1.18×10^0
	M2C	–0.1	–	0	1.06×10^0
	M2D	0.1	–	0	9.46×10^{-1}
	M2E	0.3	–	0	8.47×10^{-1}
Choice III (α_M)	M3A	–0.5	–	0	3.57×10^8
	M3B	–0.3	–	0	1.35×10^5
	M3C	–0.1	–	0	5.12×10^1
	M3D	–0.01	–	0	1.48×10^0
	M3E	0.1	–	0	1.95×10^{-2}
	M3F	0.3	–	0	7.48×10^{-6}

Table 1: Parameters used for the numerical studies: for all runs, $k_1 = 10^{-3}$ is the smallest wave number and $N = 46\,000$ is the number of grid points in one dimension. $\mathcal{E}_{\text{GW}}/\mathcal{E}_{\text{GW}}^*$ indicates the present-day values of the energy density due to MG with respect to the corresponding GR values. For each of the runs in series M0 and M3, we have performed an additional run with $k_1 = 10^{-7}$ to study the spectral modifications at even smaller k .

shallower at smaller k . The position of this spectral change is a fixed fraction of the Hubble horizon at the time of generation, determined by the value of α_M^* , that does not depend on the specific value of η_* . Finally, the time of generation determines the range of frequencies where we observe the signal as well as its amplitude via equation (3.16).

The amplitude $S_{h'}^*$ and the position of the peak k_* can be chosen to represent a specific model. For example, the values $S_{h'}^* = 5 \times 10^{-10}$ and $k_* = 10$ are used in our runs (see table 1) and they would produce a normalized initial total energy density⁷ $\mathcal{E}_{\text{GW}} \simeq 10^{-9}$,

⁷The turbulent and GW energy densities are normalized to the radiation energy density, such that \mathcal{E}_{GW} during RD can be computed as

$$\mathcal{E}_{\text{GW}}(\eta) = \frac{1}{6} \int_0^\infty S_{h'}(k, \eta) dk.$$

For the spectral shape $S_{h'}(k)$ given in equation (5.1) with $k_* = 10$, one finds $\mathcal{E}_{\text{GW}} \simeq 2S_{h'}^*$ (see the associated online material [74]).

which corresponds to a vortically turbulent source with an energy density of roughly $q\mathcal{E}_{\text{turb}}^* \simeq 1.74 \times 10^{-4}$. This is related via

$$\mathcal{E}_{\text{GW}}^* = (q\mathcal{E}_{\text{turb}}^*/k_s)^2, \quad (5.2)$$

where q is an empirically determined coefficient for a specific type of turbulence source $\mathcal{E}_{\text{turb}}^*$, and is found to be of the order of unity or larger (up to ~ 5), depending on the production mechanism of the source [79, 81, 82], and k_s is the characteristic scale of the turbulence sourcing, which is related to k_* in equation (5.1) as $k_* \simeq 1.143 \times 1.6 k_s \simeq 1.83 k_s$, where the factor 1.143 relates the position of the maximum of $\Omega_{\text{GW}}(k) \propto k S_{h'}(k)$ and k_* (see the associated online material [74]) and 1.6 the relation between k_s and the maximum [84].

5.2 Time evolution

For constant $\alpha_{\text{T}} \neq 0$ and $\alpha_{\text{M}} = 0$, the GW energy density stays constant in time and its magnitude is modified by the specific value of α_{T} , as it can be predicted from the analytical solution to equation (2.3) in the absence of sources during RD, given in equation (3.20) under the WKB approximation. We find excellent agreement between the WKB estimate and the numerical solution of the GW energy density. Note that this corresponds to a boost of energy for $\alpha_{\text{T}} > 0$ and a depletion for $\alpha_{\text{T}} < 0$, given by $1 + \frac{1}{2}\alpha_{\text{T}}$. Hence, the relative changes upon the GR solutions are of order $\alpha_{\text{T}} \sim \mathcal{O}(10^{-1})$ (see table 1), which would become much smaller if we restrict α_{T} to the present-time constraint at the LIGO–Virgo frequency band $\alpha_{\text{T},0} \lesssim \mathcal{O}(10^{-15})$.

Figure 3 presents the time evolution of the total GW energy density $\mathcal{E}_{\text{GW}}(\eta)$ of the runs in series M0 (upper left), M1 (upper right), M2 (lower left), and M3 (lower right). In these runs, α_{M} follows each of the parameterizations given in equation (4.2) and $\alpha_{\text{T}} = 0$. Regardless of the specific parameterization, the numerical solutions and the WKB approximations agree on the total GW energy density time dependence, enhanced or depleted by a factor $e^{-2\mathcal{D}}$ for negative or positive values of $\alpha_{\text{M},0}$, respectively.

Choices 0 and III yield similar results, with a time evolution $\mathcal{E}_{\text{GW}}(\eta) \sim \eta^{-\alpha_{\text{M},0}}$ and $\mathcal{E}_{\text{GW}}(\eta) \sim \eta^{-1.5\alpha_{\text{M},0}}$ during RD era, and $\mathcal{E}_{\text{GW}} \sim \eta^{-2\alpha_{\text{M},0}}$ and $\mathcal{E}_{\text{GW}}(\eta) \sim \eta^0$ during MD, respectively. This agrees with the expectation since choice III mostly differs from choice 0 during MD. During RD, both parameterizations are almost the same and just differ by a factor $1/(1 - \Omega_{\text{mat},0}) \simeq 1.46$, leading to the different scalings. In other words, the evolution of \mathcal{E}_{GW} , proportional to $a^{-\alpha_{\text{M}}}$ when α_{M} is constant (e.g., for choice 0, and for choice III during RD era), is determined by the cosmic expansion itself. Note that choices 0 and III induce an enhancement or suppression in the total energy density that heavily depends on the values of $\alpha_{\text{M},0}$, i.e., $\mathcal{E}_{\text{GW}}/\mathcal{E}_{\text{GW}}^*$ can range from $\mathcal{O}(10^{-5})$ (choice 0) and $\mathcal{O}(10^{-6})$ (choice III) for $\alpha_{\text{M},0} = 0.3$ to $\mathcal{O}(10^7)$ (choice 0) and $\mathcal{O}(10^8)$ (choice III) for $\alpha_{\text{M},0} = -0.5$. In general, choice III leads to a larger modification due to larger values of α_{M} during RD than choice 0. The potential implications of such a large GW energy density enhancement are discussed in section 6.

For both choices I and II (see the upper right and lower left panels of figure 3), the modified GW solutions remain close to their GR counterparts for most of the time, and rapidly depart from GR as η enters ΛD and approaches the present day. This is expected since α_{M} is proportional to the scale factor and the dark energy density for choices I and II, respectively, and hence, the values of α_{M} are negligibly small for most of the cosmic history until ΛD era. For this reason, for the same values of $\alpha_{\text{M},0}$, the final values of \mathcal{E}_{GW} in both of these cases are significantly lower than those in choices 0 and III, where the modifications are accumulated from RD onward.

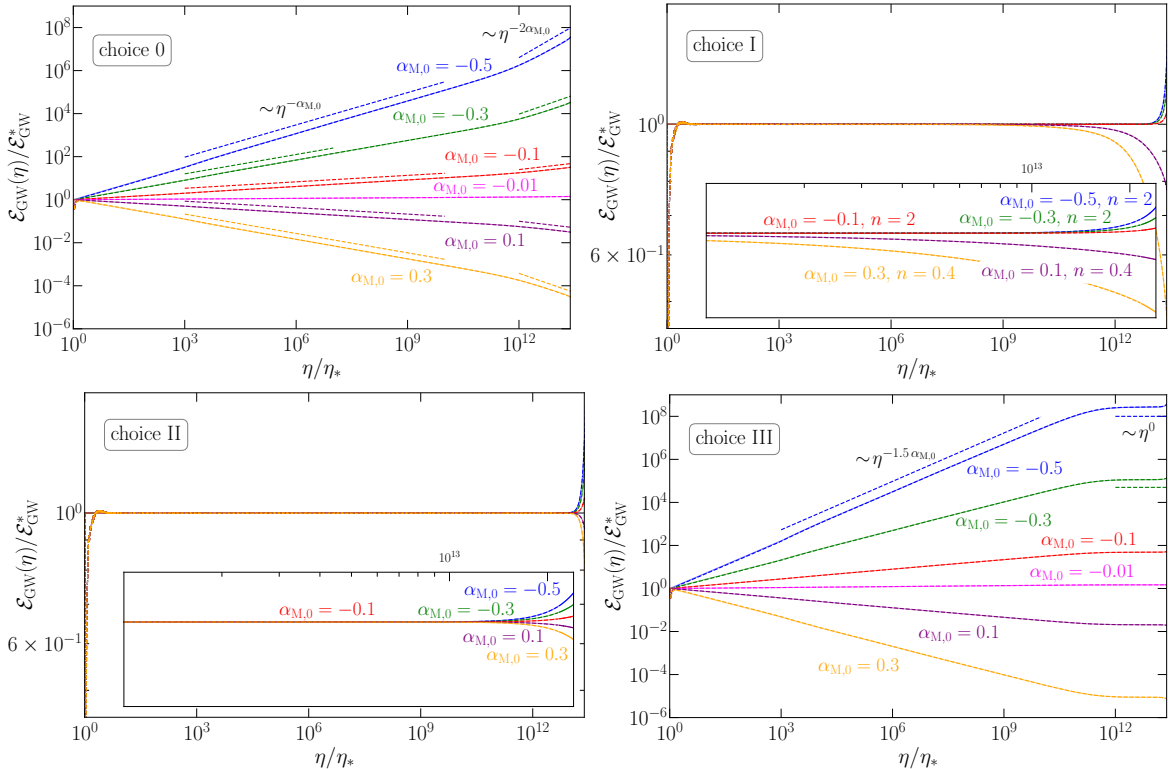


Figure 3: Time evolution of the normalized total energy density $\mathcal{E}_{\text{GW}}/\mathcal{E}_{\text{GW}}^*$ for choices 0 to III and $\alpha_{\text{M},0} \in \{-0.5, -0.3, -0.1, -0.01, 0.1, 0.3\}$. In all panels, the WKB estimates are shown as solid lines and numerical solutions as dashed lines, being almost indistinguishable. For choices I and II, the inset corresponds to the ΛD era, when there are relevant modifications to the GR solution $\mathcal{E}_{\text{GW}}^*$. All runs are initialized at the EWPT such that the present time is $\eta_0/\eta_* \simeq 2.4 \times 10^{13}$.

In figure 3, the differences between the WKB and the numerical solutions are indistinguishable. We quantify in figure 4 the relative error between the two, defined to be $\varepsilon^{\text{WKB}}(\mathcal{E}_{\text{GW}}) \equiv [\mathcal{E}_{\text{GW}}^{\text{WKB}}(\eta) - \mathcal{E}_{\text{GW}}(\eta)]/\mathcal{E}_{\text{GW}}(\eta)$. In all panels, there exists a brief but relatively large error, amounting to $\lesssim 15\%$, around the initial time η_* . This is due to the sinusoidal oscillations of each k mode that are present in GR and MG alike [see equation (3.8)]. It is a consequence of setting an already saturated spectra $S_{h'}(k)$ as the initial condition at time η_* and hence, it is not due to the WKB estimate. After the initial oscillations settle down, $\varepsilon^{\text{WKB}}(\mathcal{E}_{\text{GW}})$ for choices 0 and III decrease over the majority of time in RD era. Although they both increase somewhat later on, the maximum error at the final time is only $\varepsilon^{\text{WKB}}(\mathcal{E}_{\text{GW}}) \sim 3\%$. For choices I and II, due to the negligible impact of α_{M} during RD, the GW solutions settle down to the same magnitude after the initial oscillations. Therefore, the relative errors during RD remain close to zero. During ΛD , the errors grow as the effects of α_{M} become more significant. But this is also limited, since at most $\varepsilon^{\text{WKB}}(\mathcal{E}_{\text{GW}}) \sim 1\%$ is found at the present day, lower than in choices 0 and III.

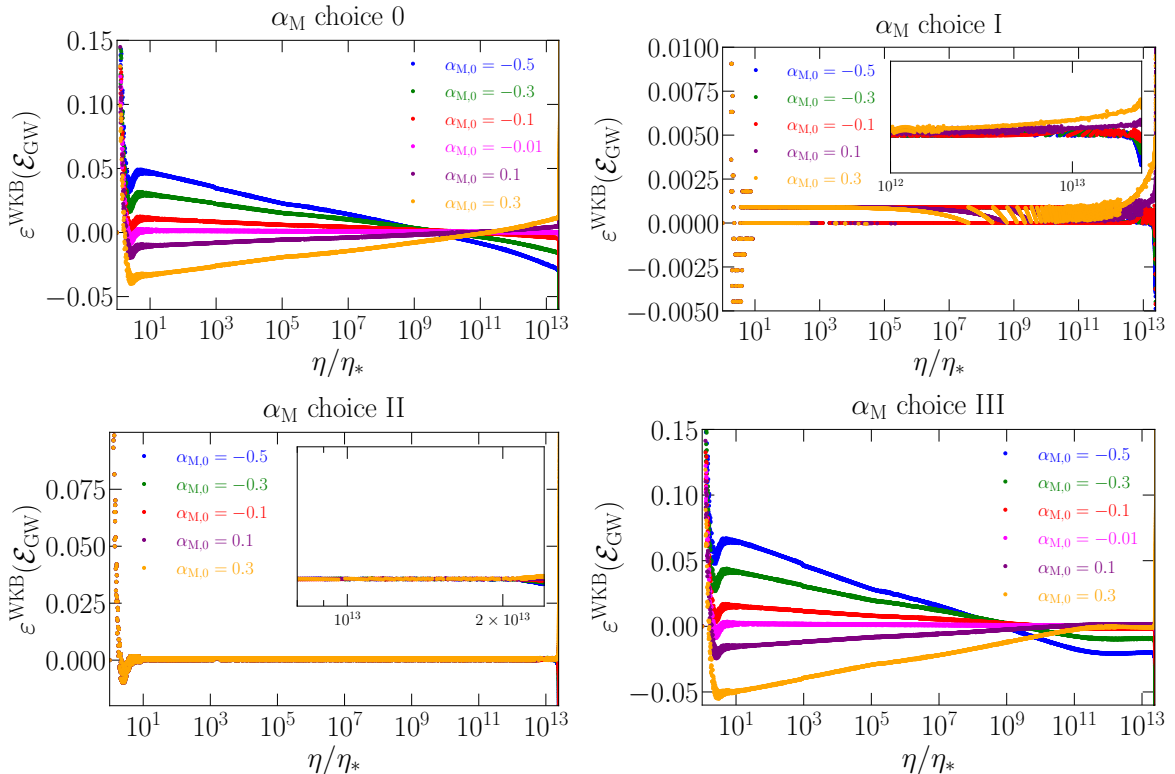


Figure 4: Relative error on the time series in figure 3 of the WKB approximation compared to the numerical simulations, $\varepsilon^{\text{WKB}}(\mathcal{E}_{\text{GW}})$.

5.3 Energy spectrum

In figure 5, we show the final energy spectrum averaged over oscillations and compensated by the factor $e^{-2\mathcal{D}}$ to study the changes on the spectral shape. The saturated spectra are shown for the choices 0 and III of α_{M} parameterization, since the rest of runs (α_{T} choice 0, α_{M} choices I and II) exhibit the same spectral shape as in GR. To study the spectral changes, we again define $\xi(k) = e^{2\mathcal{D}} S_{h'}(k) / S_{h'}^{\text{GR}}(k)$, in analogy to equation (3.18). As a reminder of the potential limitations of the WKB approximation, we mark with thin vertical lines the values of $k_{\text{lim}, \alpha''}^{\text{EW}}$ and $k_{\text{lim}, \alpha_{\text{M}}}$, and note that the latter occurs at wave numbers larger than the IR regime characterized by $k_{\text{crit}} = \frac{1}{2} |\alpha_{\text{M}}^*|$.

Comparing the numerical results to the expected spectra obtained using the WKB approximation (see figure 2), we note two main differences. In the first place, we find an IR enhancement $\xi(k) \sim k^{-\beta_0}$ with $\beta_0 \in (1, 2)$, where $\beta_0 = 2$ corresponds to the WKB approximation, for negative values of $\alpha_{\text{M},0}$, whereas for positive values there are more moderate modifications with $\beta_0 \lesssim 0.5$. Moreover, even for negative $\alpha_{\text{M},0}$, the modifications to the spectral shape are different than those predicted by the WKB estimate. These modifications can be seen more clearly in figure 6, where the left panel shows the numerically obtained $\xi(k)$ and the right panel directly presents the spectral slopes of the compensated spectra $\beta \equiv -\partial \log \xi(k) / \partial \log k$, measured at each wave number.

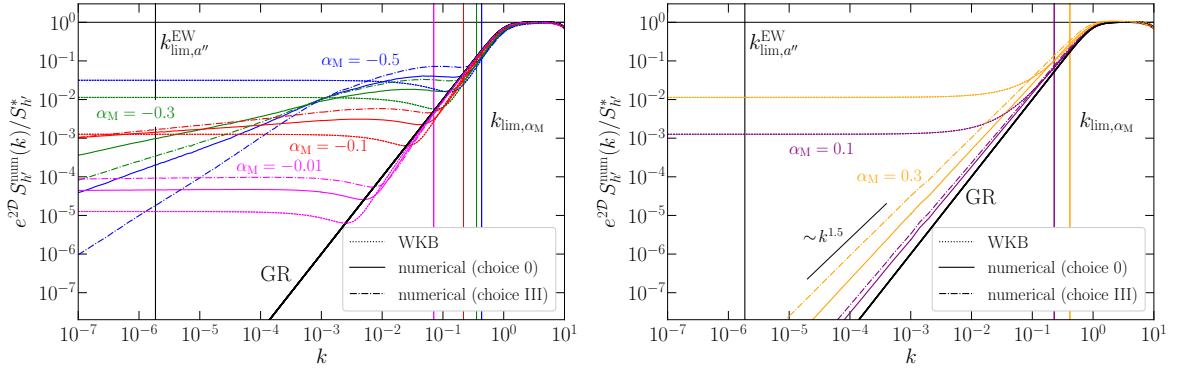


Figure 5: Saturated final energy spectra compensated by the change on the total GW energy density $e^{2D} S_{h'}^{\text{num}}(k)/S_{h'}^*$ for the numerical runs with the choices 0 and III of $\alpha_{M,0}$ parameterization. Left and right panels represent negative and positive values of $\alpha_{M,0}$, respectively. The GR solution and WKB approximation are shown in black solid and color dotted lines, respectively. Numerical solutions are shown in solid (choice 0) and dash-dotted (choice III) lines. Thin vertical lines indicate the corresponding limits to the WKB approximation $k_{\text{lim}, a''}^{\text{EW}}$ and k_{lim, α_M} . The horizontal lines show the values at the peak $S_{h'}^*$.

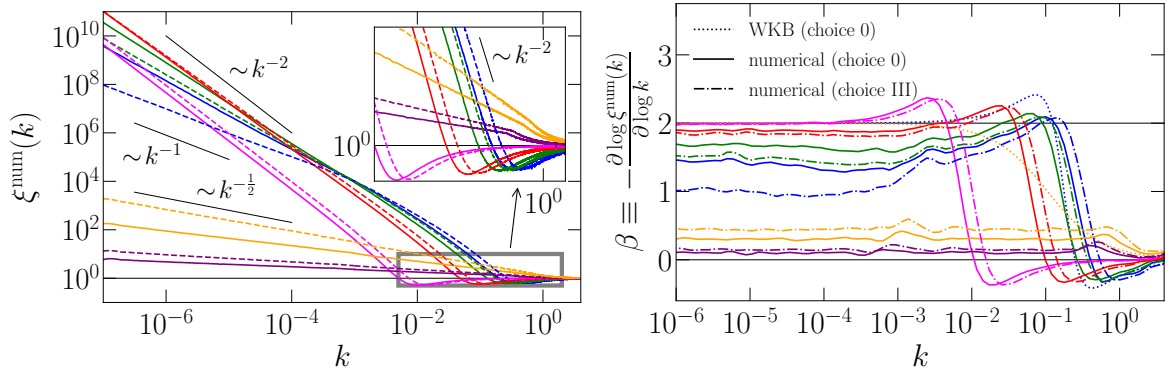


Figure 6: Left and right panels respectively show $\xi^{\text{num}}(k)$, the saturated spectra normalized with the GR solution, and β , its spectral slope as a function of $\alpha_{M,0}$. We show, for comparison, the slopes β predicted by the WKB estimate for $\alpha_{M,0} = -0.5$ and 0.3 . The horizontal thin black lines indicate the GR solution in the left panel and the slopes 0 and 2 in the right panel, for reference. Different values of $\alpha_{M,0}$ and line colors are consistent with the ones used in figures 3–5.

The slope β of the WKB estimate can be computed from equation (3.20) as

$$\beta = \frac{2\alpha_M^*(\alpha_M^* + 2k)}{8k^2 + \alpha_M^{*2} + 4k\alpha_M^*}, \quad (5.3)$$

which has an initial departure $\beta < 0$ for $\alpha_M^* < 0$ as k decreases until it reaches a peak $\beta_{\text{min}} = 1 - \sqrt{2} \simeq -0.41$ at $k_{\beta_{\text{min}}} = \frac{1}{4}\alpha_M^*\sqrt{2}/(1 - \sqrt{2}) \simeq 0.85|\alpha_M^*|$. It then grows again to zero at k_{crit} and continues to increase up to $\beta_{\text{max}} = 1 + \sqrt{2} \simeq 2.41$ at $k_{\beta_{\text{max}}} = -\frac{1}{4}\alpha_M^*\sqrt{2}/(1 + \sqrt{2}) \simeq 0.15|\alpha_M^*|$, crossing the aforementioned IR enhanced slope of -2 at the wave number $k_{\beta=-2} = \frac{1}{4}|\alpha_M^*|$ (for details, see the associated online material [74]). Finally, the slope becomes

slightly shallower and asymptotically tends to -2 as $k \rightarrow 0$, as can be seen by taking the limit in equation (5.3). For positive values of α_M^* , the slope β monotonically increases from 0 to 2 with decreasing k so it does not present any local minima or maxima. The slope β for $\alpha_M^* = -0.5$ and 0.3 under the WKB estimate is shown in the right panel of figure 6 for comparison with the numerical results.

At wave numbers close to where the IR regime starts, $k \lesssim k_{\text{crit}}$, the k^{-2} enhancement is reproduced by the numerical results for negative $\alpha_{M,0}$, flattening that part of the original GR spectrum to k^0 (see figure 5). But as k decreases, the numerical spectra exhibit slopes steeper than k^0 , closer to the original GR k^2 spectrum, that are not predicted by the WKB approximation, which maintains the k^0 slope throughout all scales $k \lesssim k_{\text{crit}}$. The departure in the IR regime occurs at different scales depending on the values of $\alpha_{M,0}$. For $\alpha_{M,0} = -0.01$, this is the least obvious, where the enhanced spectrum still keeps a roughly k^0 shape even at $k \ll k_{\text{crit}}$. For $\alpha_{M,0} = -0.5$, however, the difference becomes visible when k is still relatively close to the start of the IR regime at $k \sim k_{\text{crit}}$. We characterize the differences of the numerical results with those from the WKB estimate in table 2 by computing the critical k at which $\beta = 2$, $k_{\beta=2}^{\text{crit}}$. Under WKB this only occurs at $\frac{1}{4}|\alpha_M^*|$ and in the limit $k \rightarrow 0$ while in the simulations it occurs at a similar k and then again at a larger but finite scale $k_{\beta=2}^{\text{crit},2}$, when the spectra becomes steeper (with respect to the flat spectrum induced by $\xi^{\text{WKB}}(k) \sim k^{-2}$). We also give the final slope β_0 , such that $\xi(k) \sim k^{-\beta_0}$ as $k \rightarrow 0$.

On the other hand, for positive $\alpha_{M,0}$, the IR enhancement predicted by the WKB estimate is not observed in the numerical results. In this case, the modified spectra present small increases around $k \gtrsim 1$ and slightly shallower slopes than their GR counterparts at all superhorizon scales, characterized by $\beta_0 \gtrsim 0$.

Finally, to quantify the departures of the WKB approximation from the numerical solutions, especially at $k \leq k_{\text{lim}, \alpha_M}$, we show the relative errors in the saturated spectra as $\varepsilon^{\text{WKB}}(S_{h'}) \equiv [S_{h'}(k)^{\text{WKB}} - S_{h'}(k)]/S_{h'}(k)$ in figure 7. We observe that for positive values of $\alpha_{M,0}$, the errors grow monotonically as k becomes smaller. In fact, $\varepsilon^{\text{WKB}}(S_{h'}) \sim k^{-2}$ is found due to a consistent disagreement between the flat spectra predicted by the WKB formalism and $k^{-\beta_0}$ with $\beta_0 \gtrsim 0$ obtained numerically (see table 2). On the other hand, for negative values of $\alpha_{M,0}$, $\varepsilon^{\text{WKB}}(S_{h'})$ also increase as k becomes smaller. But since $\alpha_{M,0} < 0$ still produces a similar IR enhancement than that predicted by the WKB, the slope in the error spectrum does not become as steep as k^{-2} and depends on the corresponding values of β_0 in table 2. In all of the runs, the errors are bounded by $\lesssim 15\%$ at $k \gtrsim k_{\text{lim}, \alpha_M}$, where the WKB estimate is expected to be valid.

6 Observational implications

To infer the observational prospects of detecting a modified GW background, we convert the linear energy spectrum $S_{h'}(k)$ directly obtained from the code to the commonly used logarithmic energy spectrum $\Omega_{\text{GW}}(f)$ via equation (3.16). As a result, the GR solution in the form of the double broken power law used in the numerical simulations, i.e., $S_{h'}(k) \propto k^2$, k^0 , and $k^{-\frac{11}{3}}$ in the low, intermediate, and high wave number regimes, given by the smoothed double broken power law in equation (5.1), becomes $\Omega_{\text{GW}}(f) \propto f^3$, f , and $f^{-\frac{8}{3}}$, respectively. The normalized wave numbers used in the code are converted to the present-day physical frequencies via

$$f = \frac{c_{\text{T}} k \mathcal{H}_*}{2\pi} \frac{a_*}{a_0}, \quad (6.1)$$

	$\alpha_{M,0}$	WKB	Choice 0 (α_M)	Choice III (α_M)
$k_{\beta=2}^{\text{crit}}$	-0.5	1.25×10^{-1}	1.32×10^{-1}	1.79×10^{-1}
	-0.3	7.5×10^{-2}	9.04×10^{-2}	1.20×10^{-1}
	-0.1	2.5×10^{-2}	3.83×10^{-2}	5.16×10^{-2}
	-0.01	2.5×10^{-3}	4.58×10^{-3}	6.63×10^{-3}
$k_{\beta=2}^{\text{crit},2}$	-0.5	0	6.73×10^{-2}	9.93×10^{-2}
	-0.3	0	3.09×10^{-2}	5.54×10^{-2}
	-0.1	0	4.42×10^{-3}	9.62×10^{-3}
	-0.01	0	5.04×10^{-5}	7.44×10^{-5}
β_0	-0.5	2	1.38	0.95
	-0.3	2	1.66	1.47
	-0.1	2	1.89	1.84
	-0.01	2	2.00	1.99
	0.1	2	0.10	0.15
	0.3	2	0.30	0.44

Table 2: Spectral features in the IR regime for the values of $\alpha_{M,0}$ used in the numerical runs of table 1 and for choices 0 and III. $k_{\beta=2}^{\text{crit}}$ and $k_{\beta=2}^{\text{crit},2}$ indicate the wave numbers at which the spectral slope becomes -2 , which occurs at $k_{\beta=2} = \{0, \frac{1}{4}|\alpha_M^*|\}$ for the WKB estimate. β_0 is the asymptotic slope in the numerical runs, such that $\xi(k) \sim k^{-\beta_0}$ at large scales, which corresponds to $\beta_0 = 2$ for the WKB estimate.

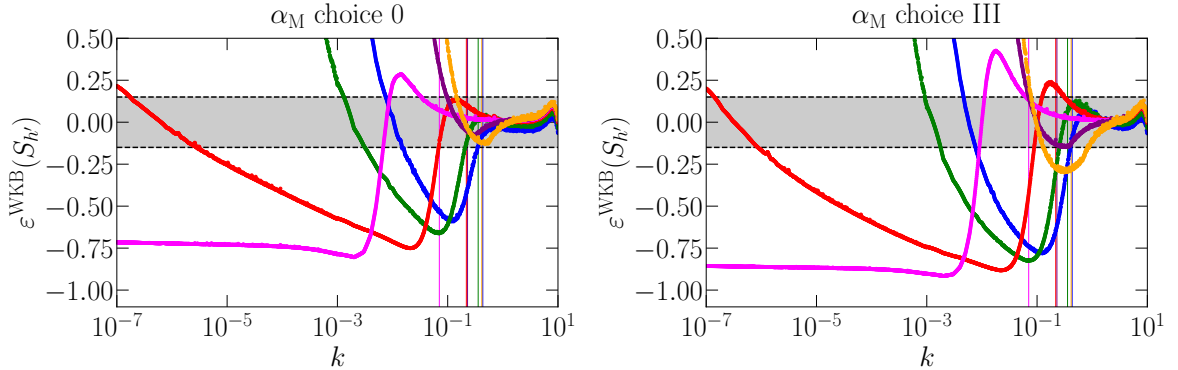


Figure 7: Relative error $\varepsilon^{\text{WKB}}(S_{h'})$ in the saturated spectra at late times of the WKB approximation compared to the numerical simulations. The vertical lines correspond to the wave number k_{lim, α_M} , below which the WKB estimate is expected to break down. The gray shaded regions in both panels represent relative errors of $\leq 15\%$. Different values of $\alpha_{M,0}$ and line colors are consistent with the ones used in figures 3–5.

where \mathcal{H}_* and a_*/a_0 are given in equations (A.8) and (A.9) and depend on the time at which the GWs are generated. The term c_T appears in equation (6.1) due to the modified dispersion relation at present time. We have found that only α_M introduces spectral changes, so we focus on the cases with $c_T = 1$. However, modified theories of gravity with $c_T \neq 1$ would allow the resulting GW spectra $\Omega_{\text{GW}}(f)$ to be shifted in f by c_T .

Assuming that the origin of the GWs is the EWPT and that the characteristic scale of the source is $\mathcal{H}_*\lambda_s = 10^{-2}$ (given, for example, by the mean separation of the broken-phase

bubbles in a first-order EWPT [102]), then $\Omega_{\text{GW}}(f)$ today peaks around the mHz band, which corresponds to the peak sensitivity of the Laser Interferometer Space Antenna (LISA). On the other hand, if the GW signal is produced at the QCDPT with a characteristic length scale of the order of the Hubble scale $\mathcal{H}_* \lambda_s \approx 1$, then it would be compatible [84] with the recent observations by the different pulsar timing array (PTA) collaborations [103–106] in the nHz band of frequencies, which are, however, not yet confirmed to correspond to a GW background. In particular, for a signal produced from MHD turbulence, the peak is estimated to occur at $k_{\text{GW}} \simeq 1.6 \times 2\pi/(\mathcal{H}_* \lambda_s)$ [84], which is obtained by taking $k_* \simeq 0.875 k_{\text{GW}}$ in equation (5.1).

Choosing the cases with the most pronounced modifications, we show in figure 8 the resulting $\Omega_{\text{GW}}(f)$ of the runs using the choice III of α_{M} parameterizations, i.e., the runs of series M3; see table 1, for the cases in which the GW signal is produced at the EWPT and at the QCDPT. For observational comparisons, we show the power law integrated sensitivity (PLIS) curves [107] of proposed future detectors such as Square Kilometer Array (SKA) [108], DECI-hertz Interferometer Gravitational wave Observatory (DECIGO) [109], Big Bang Observer [110], LISA [111], and Einstein Telescope (ET) [112].

Due to the factor $e^{-2\mathcal{D}}$, negative values of $\alpha_{\text{M},0}$ boost the GW spectral amplitude, which increases the chance of GW detection. Hence, the (non-)observation of a GW signal could serve as a constraint on the value of $\alpha_{\text{M},0}$. However, the present-day amplitude of the GW spectrum is degenerate with respect to the value of $e^{-2\mathcal{D}}$ at present time (shown in figure 9, it depends on $\alpha_{\text{M},0}$, the time-dependent parameterization of α_{M} , and the time of generation of the GWs) as well as the GW energy density produced at the time of generation $\mathcal{E}_{\text{GW}}^*$. We show in figure 8, for different values of $\alpha_{\text{M},0}$, the expected spectra at present time obtained for fixed values $e^{-2\mathcal{D}}(\eta_0) \mathcal{E}_{\text{GW}}^* \simeq 2.5 \times 10^{-7}$ and 4.44×10^{-1} at the EWPT with $k_s = 2\pi/(\mathcal{H}_* \lambda_s) \simeq 600$, which correspond to the spectral peaks at present time $h^2 \Omega_{\text{GW}} \simeq 2.34 \times 10^{-12}$ and 4.15×10^{-6} at 2.5 mHz. Note that the former amplitude would correspond to $q\mathcal{E}_{\text{turb}}^* \simeq 0.3$ in GR while the latter would be $q\mathcal{E}_{\text{turb}}^* \simeq 400$. This is completely unrealistic in GR while in MG, it would again be compatible with $q\mathcal{E}_{\text{turb}}^* \simeq 0.3$ if $e^{-2\mathcal{D}}(\eta_0) \simeq 2 \times 10^6$ that can be obtained if $\alpha_{\text{M},0} \approx -0.3$ (see choice III in figure 9). In this case, the GW signal could be amplified by MG such that the low-frequency tail could become detectable by SKA and the different PTA collaborations in the future, in a way that would break the degeneracy by a potential observation over different frequency bands. At the nHz frequencies, the f^3 branch is modified to a different slope that depends on the value of α_{M}^* at the time of generation, yielding a potential indirect observation of the MG parameter during RD era. The non-observation of such a signal at nHz frequencies would similarly constrain the value of α_{M}^* if a compatible signal is observed by LISA. Otherwise, only the product $e^{-2\mathcal{D}}(\eta_0) \mathcal{E}_{\text{GW}}^*$ could be constrained by not detecting such a signal in the LISA band. Similarly, an even larger amplification $e^{-2\mathcal{D}}(\eta_0) \mathcal{E}_{\text{GW}}^* \simeq 50$ could in principle allow the large frequency branch $f^{-8/3}$ to fall into ET sensitivity. Hence, ET could also be used to put upper bounds on the amplifications, although less stringent than those combining LISA and SKA.

For the QCDPT, we take the fixed value $e^{-2\mathcal{D}}(\eta_0) \mathcal{E}_{\text{GW}}^* \simeq 5 \times 10^{-4}$ with $k_s \simeq 10$, which corresponds to a spectral peak $h^2 \Omega_{\text{GW}} \simeq 7.4 \times 10^{-9}$ at 50.6 nHz. In GR, this corresponds to $q\mathcal{E}_{\text{turb}}^* \simeq 0.22$ so it is compatible with, for example, the primordial magnetic fields proposed in refs. [83, 84, 113] in connection to the reported PTA observations. In this case, the horizon at the QCDPT scale is within the range of frequencies where PTAs are sensitive and hence, the amplitude can be slightly modified by the value of α_{M}^* at the time of generation. Such modifications are small and at the moment, the data is not accurate enough for such a precision measurement. However, this is an interesting feature that occurs around the horizon and the

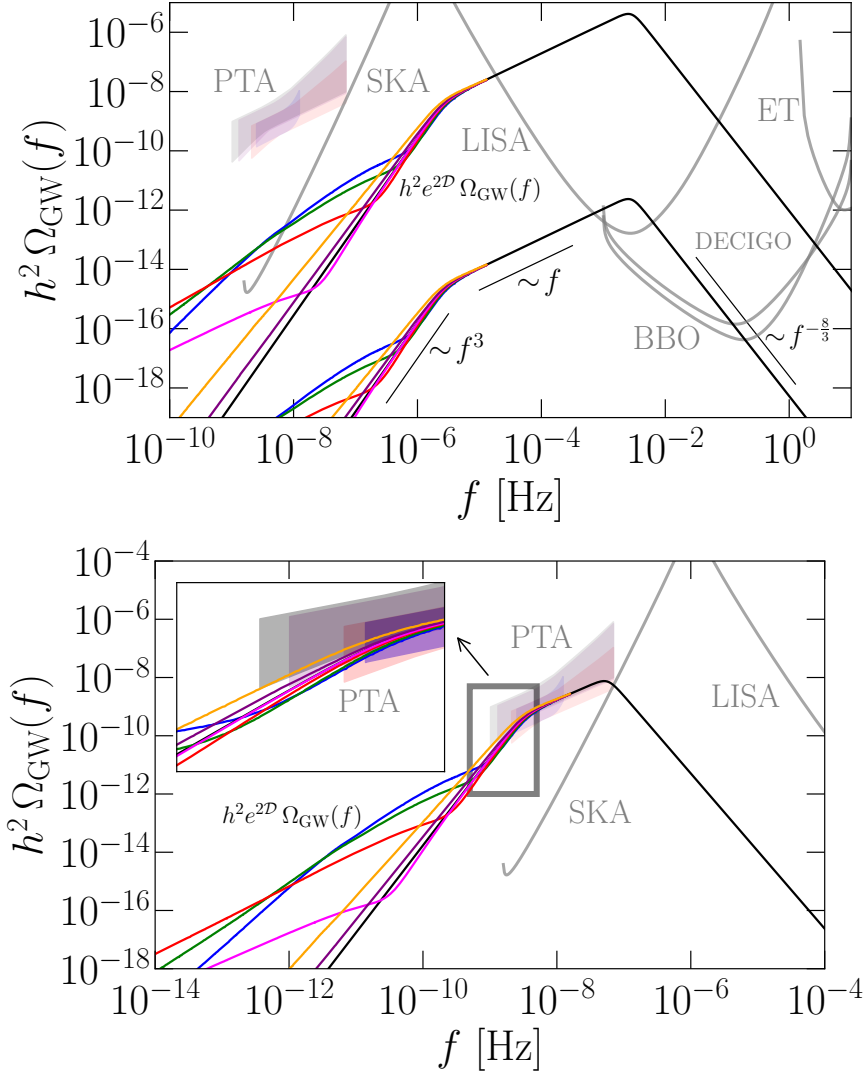


Figure 8: Present-day modified GW energy spectrum for the numerical runs of series M3 (see table 1) for GW signals produced at the EWPT (upper panel) and at the QCDPT (lower panel). GR solution is shown in black. Different values of $\alpha_{M,0}$ and line colors are consistent with the ones used in figures 3–5. Several detectors’ PLIS curves for a signal-to-noise ratio of 10 are shown in gray for comparison. The recent PTA reported observations are shown as shaded regions in blue (NANOGrav), red (PPTA), purple (EPTA), and black (IPTA) for their 2σ confidence amplitudes in the range of slopes $\gamma \geq 0$ for $\Omega(f) \sim f^\gamma$.

potential observation of a deviation with respect to the GR spectrum around the horizon scale could be an indication of non-zero α_M^* around the QCD scale. On the other hand, the current PTA observations allow us to constrain the product $e^{-2D}\mathcal{E}_{\text{GW}}^*$ for different values of k_s since we can find their values at which the GW signal would be larger than the reported PTA common-noise observations: $e^{-2D}\mathcal{E}_{\text{GW}}^* \leq 2.5 \times 10^{-3}$ for $k_s \approx 10$, $\leq 2.5 \times 10^{-2}$ for $k_s \approx 60$, $\leq 4 \times 10^{-2}$ for $k_s \approx 100$, $\leq 2.5 \times 10^{-1}$ for $k_s \approx 600$.

In addition, the expected value of $\mathcal{E}_{\text{GW}}^*$ depends on the mechanisms leading to GW production, in particular, their efficiency q , which presents a fair amount of uncertainty. Recall

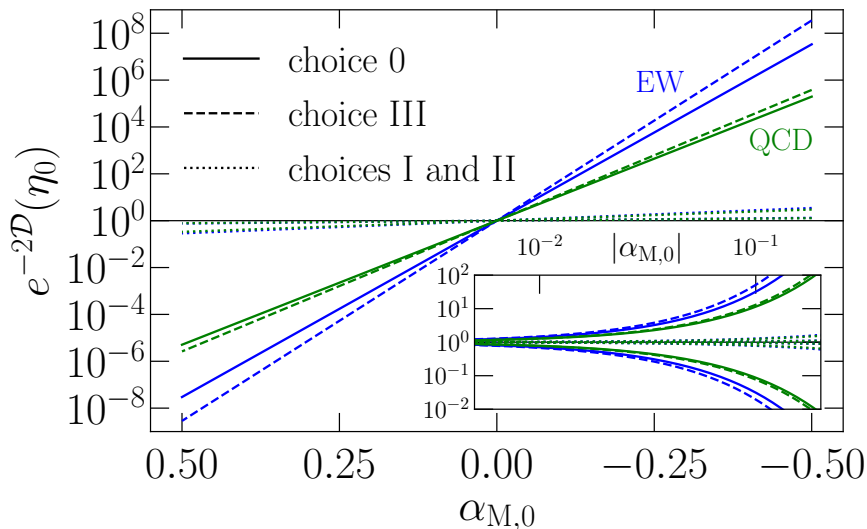


Figure 9: Total amplification or depletion factor as a function of $\alpha_{M,0}$ for a GW signal produced at the EWPT (blue) and at the QCDPT (green) for the different choices of α_M parameterization in equation (4.2).

equation (5.2), which states that the initial GW energy is determined by the initial turbulent source energy $\mathcal{E}_{\text{turb}}^*$, the production efficiency q , and the characteristic size of turbulent eddies k_s . Therefore, in practice, constraining $\alpha_{M,0}$ via its amplification effects can be rather challenging.

Finally, we note that large amplifications due to MG could potentially lead to GW signals produced at the EWPT that would dominate the sensitivity budget of various detectors, mostly LISA, but also DECIGO and BBO, for example if the product $e^{-2D}(\eta_0) \mathcal{E}_{\text{GW}}^* \sim 10^{-1}$ (see figure 8). Hence, at the moment that GW signals of astrophysical origin that propagate over a shorter period of cosmic history are detected by LISA, DECIGO and/or BBO, one can put upper bounds to $e^{-2D}(\eta_0) \mathcal{E}_{\text{GW}}^*$.

7 Conclusions

GWs in modified gravity exhibit features in their energy spectra different from what can be expected from GR. We have explored the significance of such features in terms of the spectral slopes and amplitudes in different frequency ranges, under different time-dependent functional forms and values of two modification parameters — the GW friction α_M and the tensor speed excess α_T .

We have computed the expected GW energy density spectra using the WKB approximation, and have found that the GW energy density depends on the time evolution of α_T and α_M , while its spectral shape only depends on α_M^* at the time of GW generation, and the time dependence of α_T . However, a number of limiting scales below which the WKB approximation might not hold have been identified in equations (3.12)–(3.15), motivating numerical studies to go beyond the WKB estimate, especially at superhorizon scales. For this purpose, we have performed numerical simulations using the PENCIL CODE to study the propagation of GWs along the history of the universe from their time of generation, assumed to be during the RD era, e.g., at the EWPT or at the QCDPT, until the present time.

The current-day value of the tensor speed excess is already tightly constrained by the precise measurement of the speed of GWs to $\alpha_{T,0} \lesssim \mathcal{O}(10^{-15})$. In this paper, we have found that the modifications on the GW energy density spectra introduced by a constant α_T are negligible, even when α_T takes larger values (as it might be allowed where it is not constrained, e.g., in the past or at frequencies out of the LIGO–Virgo band). In addition, α_T can modify the dispersion relation, leading to a shift in $\Omega_{\text{GW}}(f)$ by c_T . On the other hand, α_M effectively acts as an (anti-)damping term in the GW equation and can impart changes to the energy spectrum of GWs with potential implications to future observations. Considering sources of GWs at the EWPT and QCDPT, the present-day GW spectrum is expected to peak in the mHz and nHz frequency bands, respectively.

Compared to the standard GW spectra obtained in GR, the changes due to α_M are characterized by an overall boost or depletion factor $e^{-2\mathcal{D}}$, where \mathcal{D} is given in equation (3.4). However, the GW energy density at present time due to modified gravity is degenerate with the produced density at the time of generation $\mathcal{E}_{\text{GW}}^*$. Therefore, potential observations or non-observations of the GW spectra by PTA, SKA, LISA, BBO, DECIGO, ET, or others, could only place bounds on the quantity $e^{-2\mathcal{D}}(\eta_0) \mathcal{E}_{\text{GW}}^*$ and not on α_M^* or $\mathcal{E}_{\text{GW}}^*$ separately if we only consider the amplitude at the peak of the GW spectrum. For example, we have provided some upper bounds on $e^{-2\mathcal{D}}(\eta_0) \mathcal{E}_{\text{GW}}^*$ using the reported observations of a common-process spectrum over several pulsars by the different PTA collaborations; see section 6.

In addition, the GW spectrum also presents spectral modifications $\xi(k)$ around the horizon and at superhorizon scales. If $\alpha_M^* < 0$, the modification leads to an enhancement of the GW spectrum $\xi(k) \sim k^{-\beta_0}$ with $\beta_0 \in (0, 2)$, which flattens the low-frequency part of the spectrum; see table 2. The enhancement found from the numerical simulations is different than the one predicted by the WKB estimate ($\beta_0 = 2$) but it still increases the detection prospects of the low-frequency tail of the GW spectra. We also find more moderate modifications to the spectral shape around the horizon scale for all α_M^* and at all scales when $\alpha_M^* > 0$. These modifications allow us to characterize the resulting spectra due to MG.

The degeneracy between α_M and $\mathcal{E}_{\text{GW}}^*$ can be broken by observing the signal at multiple frequency bands, as α_M^* leads to a low-frequency spectral enhancement, while under GR such enhancement does not appear. This implies that, for example, a GW spectrum peaking in the mHz band can potentially have its tail in the nHz band, above PTA or SKA sensitivities. The observation of such a low-frequency tail would then be a direct indication of a non-zero α_M at the time at which the GW signal has been produced since the slope and amplitude would only depend on α_M^* .

Overall, a cosmological GW spectrum spanning many orders of magnitudes in frequency has the potential to constrain the parameter space of modified theories of gravity, especially if the modifications occur in the early universe such as the RD era.

Data availability. The source code used for the numerical solutions of this study, the PENCIL CODE, along with the additions included for the present study, is freely available [72]; see also ref. [114] for the numerical data. The calculations and the routines generating the plots are publicly available on GitHub⁸ [74].

⁸https://github.com/AlbertoRoper/GW_turbulence/tree/master/horndeski

Acknowledgments

Support through the grant 2019-04234 from the Swedish Research Council (Vetenskapsrådet) is gratefully acknowledged. Nordita is sponsored by Nordforsk. A.R.P. acknowledges support by the Swiss National Science Foundation (SNSF Ambizione grant 182044), the French National Research Agency (ANR) project MMUniverse (ANR-19-CE31-0020), and the Shota Rustaveli National Science Foundation (SRNSF) of Georgia (grant FR/18-1462). We acknowledge the allocation of computing resources provided by the Swedish National Allocations Committee at the Center for Parallel Computers at the Royal Institute of Technology in Stockholm, and by the Grand Equipement National de Calcul Intensif (GENCI) to the project ‘‘Opening new windows on Early Universe with multi-messenger astronomy’’ (A0110412058).

A Friedmann equations

Friedmann equations can be expressed in terms of the energy density $\Omega(a)$ and a smooth equation of state (EOS) $w(a)$ as

$$\frac{\ddot{a}}{a} = -\frac{1}{2}H_0^2 \Omega(a)[1 + 3w(a)], \quad \left(\frac{\dot{a}}{a}\right)^2 = H_0^2 \Omega(a), \quad (\text{A.1})$$

where $\Omega(a)$ is defined to be the ratio of total energy density to the present-day critical energy density $\rho_{\text{crit},0} \equiv 3H_0^2/\kappa$, i.e.,

$$\begin{aligned} \Omega(a) &= \frac{\rho(a)}{\rho_{\text{crit},0}} = \Omega_{\text{rad}}(a) + \Omega_{\text{mat}}(a) + \Omega_{\Lambda,0} \\ &= \left(\frac{a}{a_0}\right)^{-4} \frac{g_*}{g_*^0} \left(\frac{g_S}{g_S^0}\right)^{-\frac{4}{3}} \Omega_{\text{rad},0} + \left(\frac{a}{a_0}\right)^{-3} \Omega_{\text{mat},0} + \Omega_{\Lambda,0}. \end{aligned} \quad (\text{A.2})$$

Numerically, we take the present-time values of $\Omega_{\Lambda,0} \simeq 0.684$, $\Omega_{\text{rad},0} \simeq 4.16 \times 10^{-5} h^{-2}$, and $\Omega_{\text{mat},0} = 1 - \Omega_{\text{rad},0} - \Omega_{\Lambda,0} \simeq 0.316$, where h takes into account the uncertainties on the present-time Hubble rate $H_0 = 100 h \text{ km/s/Mpc}$. We set $h \simeq 0.67$ for the numerical studies, using the value observed by CMB experiments [6], and $g_*^0 \simeq 3.36$ and $g_S^0 \simeq 3.91$ are the reference relativistic and adiabatic degrees of freedom at the present time.⁹

The evolution of the relativistic and adiabatic degrees of freedom as a function of the temperature during RD are taken from ref. [115] and expressed as a function of a by taking $a^3 T^3 g_S$ to be constant, following an adiabatic expansion of the universe.

The characteristic EOS, corresponding to the energy density of equation (A.2), can be computed combining equations (A.1) by taking the time derivative of the second equation and introducing the first equation. This yields

$$\frac{\dot{\Omega}(a)}{\Omega(a)} = -3(1 + w)\frac{\dot{a}}{a}, \quad (\text{A.3})$$

⁹Note that neutrinos’ contribution to the radiation energy density is accounted for by taking

$$g_*^0 = 2 \left[1 + N_{\text{eff}} \frac{7}{8} \left(\frac{4}{11} \right)^{\frac{4}{3}} \right] \simeq 3.363,$$

where $N_{\text{eff}} \approx 3$, instead of $g_*^0 = 2$ at the present day due to photons only. This leads to an excess in the calculation of the radiation energy density after neutrinos become massive. However, this occurs when the radiation energy is subdominant and hence, it does not affect our calculations.

which allows us to compute $w(a)$ using equation (A.2),

$$w(a) = \left(\frac{1}{3} \Omega_{\text{rad}}(a) - \Omega_{\Lambda,0} \right) \Omega^{-1}(a). \quad (\text{A.4})$$

Equation (A.3) justifies the expected evolution of $\Omega(a)$ used in equation (A.2): approximately proportional to a^{-4} during the RD era, to a^{-3} during the MD era, and constant during ΛD . During RD, the evolution of the degrees of freedom induces some modifications with respect to the a^{-4} evolution. Equation (A.4) yields $w = 1/3$ for RD, $w = 0$ for MD, and $w = -1$ for ΛD , as expected. In the intermediate times, the functions $\Omega(a)$ and $w(a)$ transition smoothly. We can express equation (A.1) in terms of the normalized conformal time $\eta\mathcal{H}_*$ as

$$\mathcal{H} = \frac{H_0}{\mathcal{H}_*} a \sqrt{\Omega(a)}, \quad \frac{a''}{a} = \frac{1}{2} \mathcal{H}^2 [1 - 3w(a)], \quad (\text{A.5})$$

which corresponds to equation (2.9). Finally, since equation (2.5) is expressed in terms of conformal time η but equation (A.5) is still written in terms of a , we would like to substitute the variables via $a(t)$ or $a(\eta)$, which can be obtained using equation (A.1):

$$\dot{a} = H_0 a \sqrt{\Omega(a)} \Rightarrow d(H_0 t) = \frac{da}{a \sqrt{\Omega(a)}} \Rightarrow H_0(t - t_{\text{ini}}) = \int_{a_{\text{ini}}}^a \frac{da}{a \sqrt{\Omega(a)}}. \quad (\text{A.6})$$

This allows us to compute $t(a)$ and then invert the relation to obtain $a(t)$. Similarly, in conformal time, we have $dt = a d\eta$, so we solve

$$H_0(\eta - \eta_{\text{ini}}) = \int_{a_{\text{ini}}}^a \frac{da}{a^2 \sqrt{\Omega(a)}}. \quad (\text{A.7})$$

For the numerical integration, we set $a_{\text{ini}} = 10^{-20}$ at $t_{\text{ini}} = \eta_{\text{ini}} = 0$, which yields accurate results for all $a \gtrsim 10^{-19}$. Further details and numerical results to Friedmann equations can be found on the `GW_turbulence` [GitHub](#) project [74].

In the present work, we consider that the GWs are generated during a phase transition (in particular, at the EWPT or QCDPT) within the RD era. Assuming adiabatic expansion of the universe, one can compute a_*/a_0 as a function of the temperature T_* and the adiabatic degrees of freedom,

$$\frac{a_*}{a_0} = \frac{T_0}{T_*} \left(\frac{g_S^0}{g_S} \right)^{\frac{1}{3}} \simeq 7.97 \times 10^{-16} \frac{T_*}{100 \text{ GeV}} \left(\frac{g_S}{100} \right)^{-\frac{1}{3}}, \quad (\text{A.8})$$

where we take $T_0 \simeq 2.7255 \text{ K}$. Setting $a_* = 1$, such that $\mathcal{H}_* = H_*$, one gets the following value of the Hubble rate (valid during the RD era),

$$\mathcal{H}_* = \frac{\pi T_*^2}{3} \sqrt{\frac{\kappa g_*}{10}} \simeq 2.066 \times 10^{10} \text{ Hz} \left(\frac{T_*}{100 \text{ GeV}} \right)^2 \left(\frac{g_*}{100} \right)^{\frac{1}{2}}, \quad (\text{A.9})$$

with¹⁰ $\eta_* \approx \mathcal{H}_*^{-1}$. These results allow us to use the solutions from Friedmann equations and adapt them to compute the variables that appear in equations (2.3) and (2.5), normalized to the specific epoch of GW generation.

¹⁰During RD with $w = \frac{1}{3}$, $\eta = 1/\mathcal{H}$ holds exactly, but the dependence of the radiation energy density with g_* and g_S induce small deviations.

B GW energy spectrum via WKB approximation

In this section, we present the derivation of the GW spectrum obtained using the WKB approximation introduced in section 3.3. We start with the WKB solution for $\chi = e^{\mathcal{D}}h$, given in equation (3.7), and assume that at the initial time, the solution is in the free-propagating regime and follows GR¹¹, such that $|h'_*(k)| = k|h_*(k)|$,

$$\chi(k, \eta) = e^{-\tilde{\mathcal{D}}}h'_*(k) \left[\frac{1}{k} \cos k\theta + \frac{1}{kc_T^*} \left(1 + \frac{\mathcal{A}_*}{k} \right) \sin k\theta \right], \quad (\text{B.1})$$

where $\theta = \tilde{c}_T(\eta\mathcal{H}_* - 1)$ and $\mathcal{A}_* = \frac{1}{2}(\alpha_M^* + \frac{c_T'}{c_T^*})$. Its time derivative is

$$\chi'(k, \eta) = e^{-\tilde{\mathcal{D}}}h'_*(k) \left[\frac{c_T}{c_T^*} \left(1 + \frac{\mathcal{A}_*}{k} \right) \cos k\theta - c_T \sin k\theta \right] - \frac{c_T'}{2c_T} \chi(k, \eta). \quad (\text{B.2})$$

We have used that, for any function f , $[f(k\theta)]' = k\theta' f'(k\theta) = c_T k f'(k\theta)$, since $\theta' = \tilde{c}_T + \tilde{c}_T'(\eta\mathcal{H}_* - 1) = c_T$, and $\tilde{\mathcal{D}}' = c_T'/(2c_T)$. The spectrum of GWs in normalized variables, given in equation (3.16), is proportional to

$$\langle h'^2(k, \eta) \rangle = e^{-2\mathcal{D}(\eta)} \langle [\chi'(k, \eta) - \mathcal{D}'(\eta)\chi(k, \eta)]^2 \rangle, \quad (\text{B.3})$$

where the brackets indicate an average over oscillations in time. Taking into account that $\mathcal{D}' = \frac{1}{2}\alpha_M\mathcal{H}$ and using equation (B.2), the term in brackets is

$$\chi'(k, \eta) - \mathcal{D}'\chi(k, \eta) = e^{-\tilde{\mathcal{D}}}h'_*(k) \left[\mathcal{C}_1(k) \cos k\theta - \mathcal{C}_2(k) \sin k\theta \right], \quad (\text{B.4})$$

where we have defined

$$\mathcal{C}_1(k) = \frac{c_T}{c_T^*} \left(1 + \frac{\mathcal{A}_*}{k} \right) - \frac{1}{2k} \left(\frac{c_T'}{c_T} + \alpha_M\mathcal{H} \right), \quad \mathcal{C}_2(k) = c_T + \frac{1}{2kc_T^*} \left(\frac{c_T'}{c_T} + \alpha_M\mathcal{H} \right) \left(1 + \frac{\mathcal{A}_*}{k} \right). \quad (\text{B.5})$$

Hence, taking the square of equation (B.4) and averaging over oscillations in time we find

$$\langle [\chi'(k, \eta) - \mathcal{D}'\chi(k, \eta)]^2 \rangle = \frac{1}{2} e^{-2\tilde{\mathcal{D}}} \langle h'_*(k) h'_*(k) \rangle \left[\mathcal{C}_1^2(k) + \mathcal{C}_2^2(k) \right], \quad (\text{B.6})$$

where

$$\begin{aligned} \mathcal{C}_1^2(k) + \mathcal{C}_2^2(k) &= c_T^2 \left(1 + \frac{1}{c_T^{*2}} \right) + \frac{1}{k^2} \left[\frac{c_T^2 \mathcal{A}_*^2}{c_T^{*2}} + \frac{1}{4} \left(1 + \frac{1}{c_T^{*2}} \right) \left(\frac{c_T'}{c_T} + \alpha_M\mathcal{H} \right)^2 \right] \\ &\quad + \frac{2c_T^2 \mathcal{A}_*}{kc_T^{*2}} + \frac{\mathcal{A}_*}{2k^3 c_T^{*2}} \left(1 + \frac{\mathcal{A}_*}{2k} \right) \left(\frac{c_T'}{c_T} + \alpha_M\mathcal{H} \right)^2. \end{aligned} \quad (\text{B.7})$$

This expression allows us to compute the GW spectrum under the MG theory from the time evolution of α_M and c_T , and, in particular, from these values at the time of GW production,

$$\Omega_{\text{GW}}(k, \eta) = e^{-2(\mathcal{D}+\tilde{\mathcal{D}})} \Omega_{\text{GW}}^{\text{GR}}(k) \xi(k, \eta), \quad (\text{B.8})$$

¹¹We neglect here the effects of MG during the GW production and focus on the MG effects after the GWs start to propagate. Otherwise, $|h'_*(k)| \neq k|h_*(k)|$ in general and the final GW spectrum would present some additional terms. This scenario is left for future work.

where $\xi(k, \eta)$ characterizes the GW spectrum in MG with respect to the one expected under GR,

$$\begin{aligned} \xi(k, \eta) &= \frac{c_T^2}{2} \left(1 + \frac{1}{c_T^{*2}} \right) + \frac{c_T^2}{2kc_T^{*2}} \left(\alpha_M^* + \frac{c_T'^*}{c_T^*} \right) + \frac{1}{8k^3c_T^{*2}} \left(\alpha_M^* + \frac{c_T'^*}{c_T^*} \right) \left(\frac{c_T'}{c_T} + \alpha_M \mathcal{H} \right)^2 \\ &\quad + \frac{1}{8k^2} \left[\frac{c_T^2}{c_T^{*2}} \left(\alpha_M^* + \frac{c_T'^*}{c_T^*} \right)^2 + \left(1 + \frac{1}{c_T^{*2}} \right) \left(\frac{c_T'}{c_T} + \alpha_M \mathcal{H} \right)^2 \right] \\ &\quad + \frac{1}{32k^4c_T^{*2}} \left(\alpha_M^* + \frac{c_T'^*}{c_T^*} \right)^2 \left(\frac{c_T'}{c_T} + \alpha_M \mathcal{H} \right)^2. \end{aligned} \quad (\text{B.9})$$

If we set $c_T^* = c_T$ and $c_T' = c_T'^* = 0$, we recover equation (3.19)

$$\xi(k, \eta) = 1 + \frac{1}{2}\alpha_T + \frac{\alpha_M^*}{2k} + \frac{1}{8k^2} \left[\alpha_M^2 \mathcal{H}^2 \left(1 + \frac{1}{c_T^2} \right) + \alpha_M^{*2} \right] + \frac{\alpha_M^* \alpha_M^2 \mathcal{H}^2}{8k^3 c_T^2} + \frac{\alpha_M^{*2} \alpha_M^2 \mathcal{H}^2}{32k^4 c_T^2}. \quad (\text{B.10})$$

C Numerical scheme

Following refs. [73, 86], we implement a matrix solver for the modified GW equation. Equation (2.3) can be expressed as

$$h_{ij}'' + \sigma h_{ij}' + \omega^2 h_{ij} = 0, \quad (\text{C.1})$$

where

$$\sigma \equiv \alpha_M \mathcal{H}, \quad \omega^2 \equiv c_T^2 k^2 - \alpha_M \mathcal{H}^2 - \frac{a''}{a}. \quad (\text{C.2})$$

Then, assuming a solution of the type $h_{ij} = e_{ij} A e^{\lambda \eta}$ gives the characteristic equation

$$\lambda^2 + \sigma \lambda + \omega^2 = 0. \quad (\text{C.3})$$

The eigenvalues λ can be obtained as

$$\lambda_{1,2} = -\frac{1}{2} \left(\sigma \mp \sqrt{\sigma^2 - 4\omega^2} \right). \quad (\text{C.4})$$

For $\delta \eta \ll 1$, we approximate the solution by assuming that $\lambda'_{1,2} \approx \lambda''_{1,2} \approx 0$ during the time interval within time steps of the numerical solver. Then, the solution for the strains in equation (C.1) takes the form

$$h_{ij}(\eta + \delta \eta) = \mathcal{C}_{ij} e^{\lambda_1 \delta \eta} + \mathcal{D}_{ij} e^{\lambda_2 \delta \eta}, \quad (\text{C.5})$$

$$h'_{ij}(\eta + \delta \eta) = \mathcal{C}_{ij} \lambda_1 e^{\lambda_1 \delta \eta} + \mathcal{D}_{ij} \lambda_2 e^{\lambda_2 \delta \eta}, \quad (\text{C.6})$$

where \mathcal{C}_{ij} and \mathcal{D}_{ij} are constant amplitude coefficients evaluated at η . Equivalently, in matrix form, the solution can be rewritten as

$$\begin{pmatrix} h \\ h' \end{pmatrix}_{ij}^{\eta + \delta \eta} = \begin{pmatrix} e^{\lambda_1 \delta \eta} & e^{\lambda_2 \delta \eta} \\ \lambda_1 e^{\lambda_1 \delta \eta} & \lambda_2 e^{\lambda_2 \delta \eta} \end{pmatrix} \begin{pmatrix} \mathcal{C} \\ \mathcal{D} \end{pmatrix}_{ij}. \quad (\text{C.7})$$

Hence, the amplitude coefficients can be obtained as

$$\begin{pmatrix} \mathcal{C} \\ \mathcal{D} \end{pmatrix}_{ij} = \begin{pmatrix} e^{\lambda_1 \delta \eta} & e^{\lambda_2 \delta \eta} \\ \lambda_1 e^{\lambda_1 \delta \eta} & \lambda_2 e^{\lambda_2 \delta \eta} \end{pmatrix}^{-1} \begin{pmatrix} h \\ h' \end{pmatrix}_{ij}^{\eta + \delta \eta} \quad (\text{C.8})$$

$$= \frac{1}{(\lambda_2 - \lambda_1)e^{(\lambda_1 + \lambda_2)\delta \eta}} \begin{pmatrix} \lambda_2 e^{\lambda_2 \delta \eta} & -e^{\lambda_2 \delta \eta} \\ -\lambda_1 e^{\lambda_1 \delta \eta} & e^{\lambda_1 \delta \eta} \end{pmatrix} \begin{pmatrix} h \\ h' \end{pmatrix}_{ij}^{\eta + \delta \eta}, \quad (\text{C.9})$$

and, in the limit $\delta \eta \rightarrow 0$, we get

$$\lim_{\delta \eta \rightarrow 0} \begin{pmatrix} \mathcal{C} \\ \mathcal{D} \end{pmatrix}_{ij} = \frac{1}{\lambda_2 - \lambda_1} \begin{pmatrix} \lambda_2 & -1 \\ -\lambda_1 & 1 \end{pmatrix} \begin{pmatrix} h \\ h' \end{pmatrix}_{ij}^{\eta}, \quad (\text{C.10})$$

where we assume that \mathcal{C}_{ij} and \mathcal{D}_{ij} are time-independent within time steps. Therefore, the time evolution of the relevant quantities can be obtained via a matrix multiplication as

$$\begin{pmatrix} h \\ h' \end{pmatrix}_{ij}^{\eta + \delta \eta} = \mathcal{M} \begin{pmatrix} h \\ h' \end{pmatrix}_{ij}^{\eta}, \quad (\text{C.11})$$

where

$$\mathcal{M} = \frac{1}{\lambda_1 - \lambda_2} \begin{pmatrix} \lambda_1 e^{\lambda_2 \delta \eta} - \lambda_2 e^{\lambda_1 \delta \eta} & e^{\lambda_1 \delta \eta} - e^{\lambda_2 \delta \eta} \\ \lambda_1 \lambda_2 (e^{\lambda_2 \delta \eta} - e^{\lambda_1 \delta \eta}) & \lambda_1 e^{\lambda_1 \delta \eta} - \lambda_2 e^{\lambda_2 \delta \eta} \end{pmatrix}. \quad (\text{C.12})$$

In the case of $\sigma = 0$ and $\omega^2 = k^2$, the eigenvalues become $\lambda_{1,2} = \pm ik$ and the evolution matrix reduces to the one relevant for GR,

$$\mathcal{M} = \begin{pmatrix} \cos k \delta \eta & \sin k \delta \eta \\ -\sin k \delta \eta & \cos k \delta \eta \end{pmatrix}. \quad (\text{C.13})$$

D Numerical accuracy

In this section, we study the numerical accuracy of the runs. The GW solver in the PENCIL CODE has been made accurate to second order in time in the presence of a source T_{ij} under GR. However, the GW equation under modified theories of gravity lead to an equation that can be approximated within small but finite time steps under the assumption that the coefficients are constant in time, leading to the numerical solver described in section C. This method is accurate up to first order in the duration of the time step. As the coefficient variations in time become smaller, the error is also smaller, but the accuracy of the solver is still of first order. This is demonstrated in figure 10, where we show on the left panel the relative errors in the GW energy during RD and MD, and on the right panel the error during Λ D. Recall that, as introduced in section 5.1, during RD and MD, we use increasing time steps, represented by n_{incr} here. During Λ D, we use linear time steps, with the interval shown as η_{incr} in figure 10.

We also test the accuracy of the spectra in figure 11, where we show the saturated final energy spectrum for run M0A. Different colors indicate the linear time intervals during Λ D and the black curve is the spectrum obtained by running M0A entirely with increasing time steps using $n_{\text{incr}} = 0.01$. In other words, the colored curves only differ from the black one during Λ D. We observe that all of the chosen values of $\delta \eta$ produce converging energy spectra after averaging over oscillations in time, although larger values of $\delta \eta$ result in more fluctuations in the numerical spectra (see the inset in figure 11). We also note that, compared

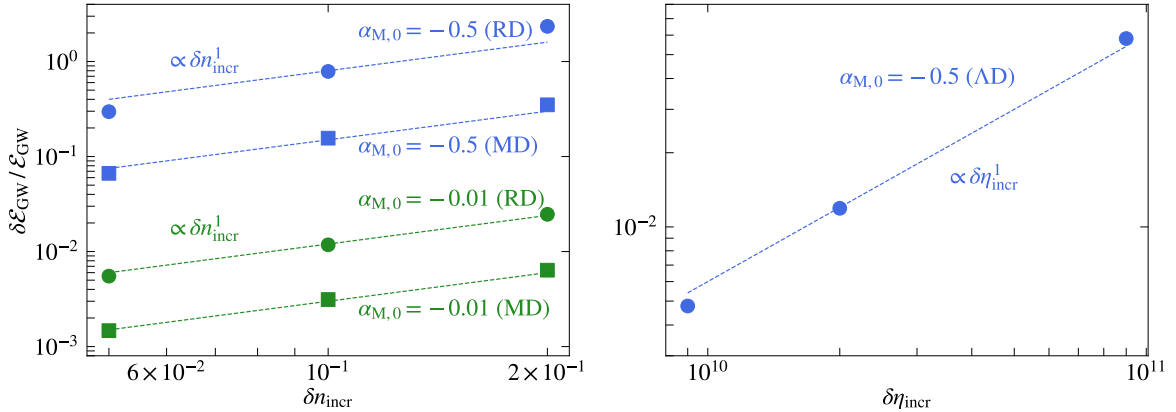


Figure 10: Relative errors as a function of the numerical time step. *Left panel:* Accuracy during RD (round dots) and MD (square dots) for $\alpha_{M,0} = -0.5$ (blue) and $\alpha_{M,0} = -0.01$ (green), where δn_{incr} indicates the difference in the time steps such that $\delta\eta = \eta \delta n_{\text{incr}}$. *Right panel:* Accuracy during ΔD with $\delta\eta = \delta\eta_{\text{incr}}$ directly indicating the linear time interval. The errors are calculated relative to the values obtained from using the smallest $\delta n_{\text{incr}} = 10^{-2}$ (left panel) and $\delta\eta_{\text{incr}} = 5 \times 10^9$ (right panel).

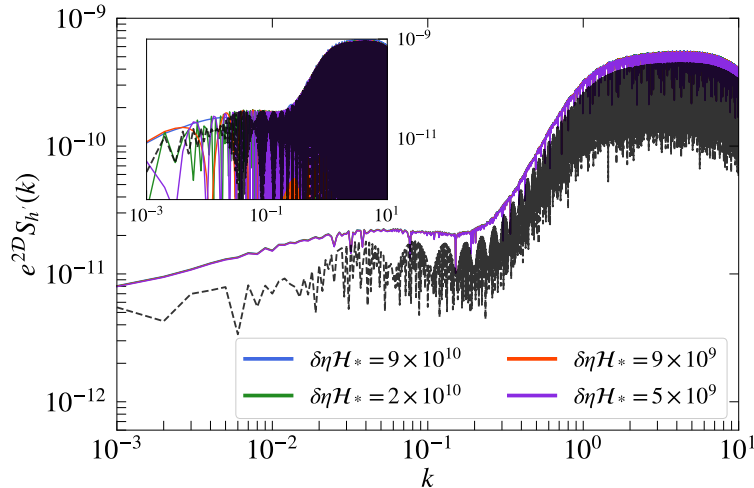


Figure 11: Saturated energy spectrum $e^{2D} S_{h'}(k)$ for $\alpha_{M,0} = -0.5$ (run M0A) with different time steps $\delta\eta \mathcal{H}_*$ during ΔD , where $n_{\text{incr}} = 0.01$ is used during RD and MD. The black dashed curves correspond to the run M0A performed entirely, i.e., including ΔD , with increasing time steps with $n_{\text{incr}} = 0.01$. The inset directly shows the spectrum at the final time without averaging over time oscillations.

to results from hybrid time steps, the entirely nonuniform time steps somewhat underestimate the final energy spectrum.

These accuracy tests justify our choice to use nonuniform time steps during RD and MD to improve the efficiency of the simulations, and uniform linear time steps (with $\delta\eta$ that already gives converged results) during ΔD .

References

- [1] A.G. Riess, S. Casertano, W. Yuan, L.M. Macri and D. Scolnic, *Large Magellanic Cloud Cepheid Standards Provide a 1% Foundation for the Determination of the Hubble Constant and Stronger Evidence for Physics beyond Λ CDM*, *Astrophys. J.* **876** (2019) 85 [1903.07603].
- [2] A.G. Riess, S. Casertano, W. Yuan, J.B. Bowers, L. Macri, J.C. Zinn et al., *Cosmic Distances Calibrated to 1% Precision with Gaia EDR3 Parallaxes and Hubble Space Telescope Photometry of 75 Milky Way Cepheids Confirm Tension with Λ CDM*, *Astrophys. J. Lett.* **908** (2021) L6 [2012.08534].
- [3] A.G. Riess et al., *A Comprehensive Measurement of the Local Value of the Hubble Constant with $1 \text{ km s}^{-1} \text{ Mpc}^{-1}$ Uncertainty from the Hubble Space Telescope and the SHOES Team*, *Astrophys. J. Lett.* **934** (2022) L7 [2112.04510].
- [4] K.C. Wong et al., *HOLiCOW – XIII. A 2.4 per cent measurement of H_0 from lensed quasars: 5.3σ tension between early- and late-Universe probes*, *Mon. Not. Roy. Astron. Soc.* **498** (2020) 1420 [1907.04869].
- [5] D.W. Pesce et al., *The Megamaser Cosmology Project. XIII. Combined Hubble constant constraints*, *Astrophys. J. Lett.* **891** (2020) L1 [2001.09213].
- [6] PLANCK collaboration, *Planck 2018 results. VI. Cosmological parameters*, *Astron. Astrophys.* **641** (2020) A6 [1807.06209].
- [7] BOSS collaboration, *The clustering of galaxies in the completed SDSS-III Baryon Oscillation Spectroscopic Survey: cosmological analysis of the DR12 galaxy sample*, *Mon. Not. Roy. Astron. Soc.* **470** (2017) 2617 [1607.03155].
- [8] L. Verde, T. Treu and A.G. Riess, *Tensions between the Early and the Late Universe*, *Nature Astron.* **3** (2019) 891 [1907.10625].
- [9] B.F. Schutz, *Determining the Hubble Constant from Gravitational Wave Observations*, *Nature* **323** (1986) 310.
- [10] D.E. Holz and S.A. Hughes, *Using gravitational-wave standard sirens*, *Astrophys. J.* **629** (2005) 15 [astro-ph/0504616].
- [11] S. Nissanke, D.E. Holz, N. Dalal, S.A. Hughes, J.L. Sievers and C.M. Hirata, *Determining the Hubble constant from gravitational wave observations of merging compact binaries*, **1307.2638**.
- [12] LIGO SCIENTIFIC, VIRGO, 1M2H, DARK ENERGY CAMERA GW-E, DES, DLT40, LAS CUMBRES OBSERVATORY, VINROUGE, MASTER collaboration, *A gravitational-wave standard siren measurement of the Hubble constant*, *Nature* **551** (2017) 85 [1710.05835].
- [13] DES collaboration, *A statistical standard siren measurement of the Hubble constant from the LIGO/Virgo gravitational wave compact object merger GW190814 and Dark Energy Survey galaxies*, *Astrophys. J. Lett.* **900** (2020) L33 [2006.14961].
- [14] A. Palmese, C.R. Bom, S. Mucesh and W.G. Hartley, *A Standard Siren Measurement of the Hubble Constant Using Gravitational-wave Events from the First Three LIGO/Virgo Observing Runs and the DESI Legacy Survey*, *Astrophys. J.* **943** (2023) 56 [2111.06445].
- [15] LISA COSMOLOGY WORKING GROUP collaboration, *Cosmology with the Laser Interferometer Space Antenna*, **2204.05434**.
- [16] M. Branchesi et al., *Science with the Einstein Telescope: a comparison of different designs*, **2303.15923**.
- [17] S. Joudaki et al., *KiDS-450 + 2dFLenS: Cosmological parameter constraints from weak gravitational lensing tomography and overlapping redshift-space galaxy clustering*, *Mon. Not. Roy. Astron. Soc.* **474** (2018) 4894 [1707.06627].

- [18] L. Perivolaropoulos and F. Skara, *Challenges for Λ CDM: An update*, *New Astron. Rev.* **95** (2022) 101659 [2105.05208].
- [19] D. Lovelock, *The Einstein tensor and its generalizations*, *J. Math. Phys.* **12** (1971) 498.
- [20] D. Lovelock, *The four-dimensionality of space and the einstein tensor*, *J. Math. Phys.* **13** (1972) 874.
- [21] G.W. Horndeski, *Second-order scalar-tensor field equations in a four-dimensional space*, *Int. J. Theor. Phys.* **10** (1974) 363.
- [22] C. Deffayet, X. Gao, D.A. Steer and G. Zahariade, *From k-essence to generalised Galileons*, *Phys. Rev. D* **84** (2011) 064039 [1103.3260].
- [23] T. Kobayashi, M. Yamaguchi and J. Yokoyama, *Generalized G-inflation: Inflation with the most general second-order field equations*, *Prog. Theor. Phys.* **126** (2011) 511 [1105.5723].
- [24] M. Zumalacárregui and J. García-Bellido, *Transforming gravity: from derivative couplings to matter to second-order scalar-tensor theories beyond the Horndeski Lagrangian*, *Phys. Rev. D* **89** (2014) 064046 [1308.4685].
- [25] J. Gleyzes, D. Langlois, F. Piazza and F. Vernizzi, *Healthy theories beyond Horndeski*, *Phys. Rev. Lett.* **114** (2015) 211101 [1404.6495].
- [26] J. Gleyzes, D. Langlois, F. Piazza and F. Vernizzi, *Exploring gravitational theories beyond Horndeski*, *JCAP* **02** (2015) 018 [1408.1952].
- [27] D. Langlois and K. Noui, *Degenerate higher derivative theories beyond Horndeski: evading the Ostrogradski instability*, *JCAP* **02** (2016) 034 [1510.06930].
- [28] J. Ben Achour, M. Crisostomi, K. Koyama, D. Langlois, K. Noui and G. Tasinato, *Degenerate higher order scalar-tensor theories beyond Horndeski up to cubic order*, *JHEP* **12** (2016) 100 [1608.08135].
- [29] D. Langlois, M. Mancarella, K. Noui and F. Vernizzi, *Effective Description of Higher-Order Scalar-Tensor Theories*, *JCAP* **05** (2017) 033 [1703.03797].
- [30] P. Hořava, *Quantum Gravity at a Lifshitz Point*, *Phys. Rev. D* **79** (2009) 084008 [0901.3775].
- [31] D. Blas, O. Pujolas and S. Sibiryakov, *Models of non-relativistic quantum gravity: The Good, the bad and the healthy*, *JHEP* **04** (2011) 018 [1007.3503].
- [32] T. Jacobson and D. Mattingly, *Gravity with a dynamical preferred frame*, *Phys. Rev. D* **64** (2001) 024028 [gr-qc/0007031].
- [33] T.G. Zlosnik, P.G. Ferreira and G.D. Starkman, *Modifying gravity with the Aether: An alternative to Dark Matter*, *Phys. Rev. D* **75** (2007) 044017 [astro-ph/0607411].
- [34] G. Tasinato, *Cosmic Acceleration from Abelian Symmetry Breaking*, *JHEP* **04** (2014) 067 [1402.6450].
- [35] L. Heisenberg, *Generalization of the Proca Action*, *JCAP* **05** (2014) 015 [1402.7026].
- [36] L. Heisenberg, R. Kase and S. Tsujikawa, *Beyond generalized Proca theories*, *Phys. Lett. B* **760** (2016) 617 [1605.05565].
- [37] E. Allys, P. Peter and Y. Rodriguez, *Generalized Proca action for an Abelian vector field*, *JCAP* **02** (2016) 004 [1511.03101].
- [38] J. Beltran Jimenez and L. Heisenberg, *Derivative self-interactions for a massive vector field*, *Phys. Lett. B* **757** (2016) 405 [1602.03410].
- [39] C. de Rham and G. Gabadadze, *Generalization of the Fierz-Pauli Action*, *Phys. Rev. D* **82** (2010) 044020 [1007.0443].

- [40] C. de Rham, G. Gabadadze and A.J. Tolley, *Resummation of Massive Gravity*, *Phys. Rev. Lett.* **106** (2011) 231101 [[1011.1232](#)].
- [41] S.F. Hassan and R.A. Rosen, *Bimetric Gravity from Ghost-free Massive Gravity*, *JHEP* **02** (2012) 126 [[1109.3515](#)].
- [42] E. Sagi, *Propagation of gravitational waves in generalized TeVeS*, *Phys. Rev. D* **81** (2010) 064031 [[1001.1555](#)].
- [43] C. Brans and R.H. Dicke, *Mach's principle and a relativistic theory of gravitation*, *Phys. Rev.* **124** (1961) 925.
- [44] B. Ratra and P.J.E. Peebles, *Cosmological Consequences of a Rolling Homogeneous Scalar Field*, *Phys. Rev. D* **37** (1988) 3406.
- [45] A. De Felice and S. Tsujikawa, *f(R) theories*, *Living Rev. Rel.* **13** (2010) 3 [[1002.4928](#)].
- [46] S.M. Carroll, A. De Felice, V. Duvvuri, D.A. Easson, M. Trodden and M.S. Turner, *The cosmology of generalized modified gravity models*, *Phys. Rev. D* **71** (2005) 063513 [[astro-ph/0410031](#)].
- [47] C. Armendariz-Picon, V.F. Mukhanov and P.J. Steinhardt, *Essentials of k essence*, *Phys. Rev. D* **63** (2001) 103510 [[astro-ph/0006373](#)].
- [48] C. Deffayet, O. Pujolas, I. Sawicki and A. Vikman, *Imperfect Dark Energy from Kinetic Gravity Braiding*, *JCAP* **10** (2010) 026 [[1008.0048](#)].
- [49] A. Nicolis, R. Rattazzi and E. Trincherini, *The Galileon as a local modification of gravity*, *Phys. Rev. D* **79** (2009) 064036 [[0811.2197](#)].
- [50] T. Clifton, P.G. Ferreira, A. Padilla and C. Skordis, *Modified Gravity and Cosmology*, *Phys. Rept.* **513** (2012) 1 [[1106.2476](#)].
- [51] E. Belgacem, Y. Dirian, S. Foffa and M. Maggiore, *Modified gravitational-wave propagation and standard sirens*, *Phys. Rev. D* **98** (2018) 023510 [[1805.08731](#)].
- [52] C. Deffayet and K. Menou, *Probing Gravity with Spacetime Sirens*, *Astrophys. J. Lett.* **668** (2007) L143 [[0709.0003](#)].
- [53] I.D. Saltas, I. Sawicki, L. Amendola and M. Kunz, *Anisotropic Stress as a Signature of Nonstandard Propagation of Gravitational Waves*, *Phys. Rev. Lett.* **113** (2014) 191101 [[1406.7139](#)].
- [54] L. Lombriser and A. Taylor, *Breaking a Dark Degeneracy with Gravitational Waves*, *JCAP* **03** (2016) 031 [[1509.08458](#)].
- [55] A. Nishizawa, *Generalized framework for testing gravity with gravitational-wave propagation. I. Formulation*, *Phys. Rev. D* **97** (2018) 104037 [[1710.04825](#)].
- [56] E. Belgacem, Y. Dirian, S. Foffa and M. Maggiore, *Gravitational-wave luminosity distance in modified gravity theories*, *Phys. Rev. D* **97** (2018) 104066 [[1712.08108](#)].
- [57] S. Mastrogiovanni, D. Steer and M. Barsuglia, *Probing modified gravity theories and cosmology using gravitational-waves and associated electromagnetic counterparts*, *Phys. Rev. D* **102** (2020) 044009 [[2004.01632](#)].
- [58] S. Mastrogiovanni, L. Haegel, C. Karathanasis, I.M.n. Hernandez and D.A. Steer, *Gravitational wave friction in light of GW170817 and GW190521*, *JCAP* **02** (2021) 043 [[2010.04047](#)].
- [59] S. Arai and A. Nishizawa, *Generalized framework for testing gravity with gravitational-wave propagation. II. Constraints on Horndeski theory*, *Phys. Rev. D* **97** (2018) 104038 [[1711.03776](#)].

- [60] LISA COSMOLOGY WORKING GROUP collaboration, *Testing modified gravity at cosmological distances with LISA standard sirens*, *JCAP* **07** (2019) 024 [[1906.01593](#)].
- [61] R. D’Agostino and R.C. Nunes, *Probing observational bounds on scalar-tensor theories from standard sirens*, *Phys. Rev. D* **100** (2019) 044041 [[1907.05516](#)].
- [62] I.S. Matos, M.O. Calvão and I. Waga, *Gravitational wave propagation in $f(R)$ models: New parametrizations and observational constraints*, *Phys. Rev. D* **103** (2021) 104059 [[2104.10305](#)].
- [63] I.S. Matos, E. Bellini, M.O. Calvão and M. Kunz, *Testing gravity with gravitational wave friction and gravitational slip*, [2210.12174](#).
- [64] LIGO SCIENTIFIC, VIRGO, FERMI-GBM, INTEGRAL collaboration, *Gravitational Waves and Gamma-rays from a Binary Neutron Star Merger: GW170817 and GRB 170817A*, *Astrophys. J. Lett.* **848** (2017) L13 [[1710.05834](#)].
- [65] T. Baker, E. Bellini, P.G. Ferreira, M. Lagos, J. Noller and I. Sawicki, *Strong constraints on cosmological gravity from GW170817 and GRB 170817A*, *Phys. Rev. Lett.* **119** (2017) 251301 [[1710.06394](#)].
- [66] J.M. Ezquiaga and M. Zumalacárregui, *Dark Energy After GW170817: Dead Ends and the Road Ahead*, *Phys. Rev. Lett.* **119** (2017) 251304 [[1710.05901](#)].
- [67] P. Creminelli and F. Vernizzi, *Dark Energy after GW170817 and GRB170817A*, *Phys. Rev. Lett.* **119** (2017) 251302 [[1710.05877](#)].
- [68] J. Sakstein and B. Jain, *Implications of the Neutron Star Merger GW170817 for Cosmological Scalar-Tensor Theories*, *Phys. Rev. Lett.* **119** (2017) 251303 [[1710.05893](#)].
- [69] C. de Rham and S. Melville, *Gravitational Rainbows: LIGO and Dark Energy at its Cutoff*, *Phys. Rev. Lett.* **121** (2018) 221101 [[1806.09417](#)].
- [70] Y. He, A. Brandenburg and A. Sinha, *Tensor spectrum of turbulence-sourced gravitational waves as a constraint on graviton mass*, *JCAP* **07** (2021) 015 [[2104.03192](#)].
- [71] M. Chevallier and D. Polarski, *Accelerating universes with scaling dark matter*, *Int. J. Mod. Phys. D* **10** (2001) 213 [[gr-qc/0009008](#)].
- [72] PENCIL CODE collaboration, *The Pencil Code, a modular MPI code for partial differential equations and particles: multipurpose and multiuser-maintained*, *J. Open Source Softw.* **6** (2021) 2807 [[2009.08231](#)].
- [73] A. Roper Pol, A. Brandenburg, T. Kahniashvili, A. Kosowsky and S. Mandal, *The timestep constraint in solving the gravitational wave equations sourced by hydromagnetic turbulence*, *Geophys. Astrophys. Fluid Dynamics* **114** (2020) 130 [[1807.05479](#)].
- [74] A. Roper Pol, *GitHub project “GW_turbulence”, doi: 10.5281/zenodo.6045844*.
- [75] C. Caprini and D.G. Figueroa, *Cosmological Backgrounds of Gravitational Waves*, *Class. Quant. Grav.* **35** (2018) 163001 [[1801.04268](#)].
- [76] J.-C. Hwang and H.-R. Noh, *Gauge ready formulation of the cosmological kinetic theory in generalized gravity theories*, *Phys. Rev. D* **65** (2002) 023512 [[astro-ph/0102005](#)].
- [77] R.C. Nunes, M.E.S. Alves and J.C.N. de Araujo, *Primordial gravitational waves in Horndeski gravity*, *Phys. Rev. D* **99** (2019) 084022 [[1811.12760](#)].
- [78] G. Tasinato, A. Garoffolo, D. Bertacca and S. Matarrese, *Gravitational-wave cosmological distances in scalar-tensor theories of gravity*, *JCAP* **06** (2021) 050 [[2103.00155](#)].
- [79] A. Roper Pol, S. Mandal, A. Brandenburg, T. Kahniashvili and A. Kosowsky, *Numerical simulations of gravitational waves from early-universe turbulence*, *Phys. Rev. D* **102** (2020) 083512 [[1903.08585](#)].

- [80] T. Kahniashvili, A. Brandenburg, G. Gogoberidze, S. Mandal and A. Roper Pol, *Circular polarization of gravitational waves from early-Universe helical turbulence*, *Phys. Rev. Res.* **3** (2021) 013193 [2011.05556].
- [81] A. Brandenburg, G. Gogoberidze, T. Kahniashvili, S. Mandal, A. Roper Pol and N. Shenoy, *The scalar, vector, and tensor modes in gravitational wave turbulence simulations*, *Class. Quant. Grav.* **38** (2021) 145002 [2103.01140].
- [82] A. Roper Pol, S. Mandal, A. Brandenburg and T. Kahniashvili, *Polarization of gravitational waves from helical MHD turbulent sources*, *JCAP* **04** (2022) 019 [2107.05356].
- [83] A. Brandenburg, E. Clarke, Y. He and T. Kahniashvili, *Can we observe the QCD phase transition-generated gravitational waves through pulsar timing arrays?*, *Phys. Rev. D* **104** (2021) 043513 [2102.12428].
- [84] A. Roper Pol, C. Caprini, A. Neronov and D. Semikoz, *Gravitational wave signal from primordial magnetic fields in the Pulsar Timing Array frequency band*, *Phys. Rev. D* **105** (2022) 123502 [2201.05630].
- [85] R. Sharma and A. Brandenburg, *Low frequency tail of gravitational wave spectra from hydromagnetic turbulence*, *Phys. Rev. D* **106** (2022) 103536 [2206.00055].
- [86] A. Brandenburg and R. Sharma, *Simulating Relic Gravitational Waves from Inflationary Magnetogenesis*, *Astrophys. J.* **920** (2021) 26 [2106.03857].
- [87] A. Brandenburg, Y. He and R. Sharma, *Simulations of Helical Inflationary Magnetogenesis and Gravitational Waves*, *Astrophys. J.* **922** (2021) 192 [2107.12333].
- [88] Y. He, A. Roper Pol and A. Brandenburg, *Leading-order nonlinear gravitational waves from reheating magnetogenesis*, [2110.14456](#).
- [89] K. Saikawa and S. Shirai, *Primordial gravitational waves, precisely: The role of thermodynamics in the Standard Model*, *JCAP* **05** (2018) 035 [1803.01038].
- [90] LISA COSMOLOGY WORKING GROUP collaboration, *Measuring the propagation speed of gravitational waves with LISA*, *JCAP* **08** (2022) 031 [2203.00566].
- [91] Y. Cai, Y.-T. Wang and Y.-S. Piao, *Is there an effect of a nontrivial c_T during inflation?*, *Phys. Rev. D* **93** (2016) 063005 [1510.08716].
- [92] Y. Cai, Y.-T. Wang and Y.-S. Piao, *Propagating speed of primordial gravitational waves and inflation*, *Phys. Rev. D* **94** (2016) 043002 [1602.05431].
- [93] S.D. Odintsov, V.K. Oikonomou and R. Myrzakulov, *Spectrum of Primordial Gravitational Waves in Modified Gravities: A Short Overview*, *Symmetry* **14** (2022) 729 [2204.00876].
- [94] E. Bellini and I. Sawicki, *Maximal freedom at minimum cost: linear large-scale structure in general modifications of gravity*, *JCAP* **07** (2014) 050 [1404.3713].
- [95] J. Kennedy, L. Lombriser and A. Taylor, *Reconstructing Horndeski theories from phenomenological modified gravity and dark energy models on cosmological scales*, *Phys. Rev. D* **98** (2018) 044051 [1804.04582].
- [96] J. Gleyzes, *Parametrizing modified gravity for cosmological surveys*, *Phys. Rev. D* **96** (2017) 063516 [1705.04714].
- [97] M. Denissenya and E.V. Linder, *Gravity's Islands: Parametrizing Horndeski Stability*, *JCAP* **11** (2018) 010 [1808.00013].
- [98] M. Yoshimura, *Stronger gravity in the early universe*, [2204.11384](#).
- [99] M. Zumalacarregui, *Gravity in the Era of Equality: Towards solutions to the Hubble problem without fine-tuned initial conditions*, *Phys. Rev. D* **102** (2020) 023523 [2003.06396].

- [100] M. Braglia, M. Ballardini, F. Finelli and K. Koyama, *Early modified gravity in light of the H_0 tension and LSS data*, *Phys. Rev. D* **103** (2021) 043528 [2011.12934].
- [101] E.V. Linder, *Gravitational Wave Distances in Horndeski Cosmology*, [2108.11526](#).
- [102] M.S. Turner, E.J. Weinberg and L.M. Widrow, *Bubble nucleation in first order inflation and other cosmological phase transitions*, *Phys. Rev. D* **46** (1992) 2384.
- [103] NANOGrav collaboration, *The NANOGrav 12.5 yr Data Set: Search for an Isotropic Stochastic Gravitational-wave Background*, *Astrophys. J. Lett.* **905** (2020) L34 [2009.04496].
- [104] B. Goncharov et al., *On the Evidence for a Common-spectrum Process in the Search for the Nanohertz Gravitational-wave Background with the Parkes Pulsar Timing Array*, *Astrophys. J. Lett.* **917** (2021) L19 [2107.12112].
- [105] S. Chen et al., *Common-red-signal analysis with 24-yr high-precision timing of the European Pulsar Timing Array: inferences in the stochastic gravitational-wave background search*, *Mon. Not. Roy. Astron. Soc.* **508** (2021) 4970 [2110.13184].
- [106] J. Antoniadis et al., *The International Pulsar Timing Array second data release: Search for an isotropic gravitational wave background*, *Mon. Not. Roy. Astron. Soc.* **510** (2022) 4873 [2201.03980].
- [107] K. Schmitz, *New Sensitivity Curves for Gravitational-Wave Signals from Cosmological Phase Transitions*, *JHEP* **01** (2021) 097 [2002.04615].
- [108] C.J. Moore, R.H. Cole and C.P.L. Berry, *Gravitational-wave sensitivity curves*, *Class. Quant. Grav.* **32** (2015) 015014 [1408.0740].
- [109] N. Seto, S. Kawamura and T. Nakamura, *Possibility of direct measurement of the acceleration of the universe using 0.1-Hz band laser interferometer gravitational wave antenna in space*, *Phys. Rev. Lett.* **87** (2001) 221103 [astro-ph/0108011].
- [110] J. Crowder and N.J. Cornish, *Beyond LISA: Exploring future gravitational wave missions*, *Phys. Rev. D* **72** (2005) 083005 [gr-qc/0506015].
- [111] C. Caprini, D.G. Figueroa, R. Flauger, G. Nardini, M. Peloso, M. Pieroni et al., *Reconstructing the spectral shape of a stochastic gravitational wave background with LISA*, *JCAP* **11** (2019) 017 [1906.09244].
- [112] M. Punturo et al., *The Einstein Telescope: A third-generation gravitational wave observatory*, *Class. Quant. Grav.* **27** (2010) 194002.
- [113] A. Neronov, A. Roper Pol, C. Caprini and D. Semikoz, *NANOGrav signal from magnetohydrodynamic turbulence at the QCD phase transition in the early Universe*, *Phys. Rev. D* **103** (2021) 041302 [2009.14174].
- [114] Y. He, A. Roper Pol and A. Brandenburg, *Datasets of "Modified propagation of gravitational waves from the early radiation era"*, doi: 10.5281/zenodo.7408601 (v2022.12.07); see also <http://norlæ65.nordita.org/~yutong/projects/Horndeski/> for easier access, .
- [115] M.B. Hindmarsh, M. Lüben, J. Lumma and M. Pauly, *Phase transitions in the early universe*, *SciPost Phys. Lect. Notes* **24** (2021) 1 [2008.09136].